Marquette University
e-Publications@Marquette

Master's Theses (2009 -)

Dissertations, Theses, and Professional Projects

Reducing Porosity in LPBF TI-6AL-4V by Parameter Optimization and Low Temperature Hot Isostatic Pressing Cycle

Penn Rawn
Marquette University

Follow this and additional works at: https://epublications.marquette.edu/theses_open

 Part of the Engineering Commons

Recommended Citation

Rawn, Penn, "Reducing Porosity in LPBF TI-6AL-4V by Parameter Optimization and Low Temperature Hot Isostatic Pressing Cycle" (2023). *Master's Theses (2009 -)*. 773.
https://epublications.marquette.edu/theses_open/773

REDUCING POROSITY IN LPBF TI-6AL-4V ALLOY BY PARAMETER OPTIMIZATION AND LOW TEMPERATURE HOT ISOSTATIC PRESSING CYCLE

By

Penn Rawn

A Thesis Submitted to the Faculty of The Graduate School,
Marquette University,
in Partial Fulfillment of the Requirements for
the Degree of Master of Science

Milwaukee, Wisconsin

August 2023

ABSTRACT
REDUCING POROSITY IN LPBF TI-6AL-4V ALLOY BYPARAMETER OPTIMIZATION AND LOW TEMPERATURE HOT ISOSTATIC PRESSING CYCLE

Penn Rawn

Marquette University, 2023

Powder bed based additive manufacturing has advantages in its ability to make specialized parts with complex geometries. Unfortunately, components made through such processes often suffer from manufacturing defects including porosity. To study pore formation and removal, specimens of Ti-6Al-4V were built at varied levels of laser power, travel speed, hatch spacing, and layer thickness to obtain a variety of initial defect populations. The specimens were then subjected to a hot isostatic pressure (HIP) at 850 ˚C and 200 *MPa* to evaluate the low temperature high pressure (LTHP) cycle's ability to remove pores. Image analysis was used to estimate the relative density of specimens in both the as-built and the post-HIP condition. A visible trend between GED (global energy density) and porosity was identified for a layer thickness of 20 μm, but not when the layer thickness was 40 μm. HIP removed most pores but was less effective at removing faceted pores.

Qualitative analysis revealed a moderate change in microstructure. Vicker's microhardness measurements showed that hardness decreased after HIP. There was a relationship between hardness and GED in the as-built condition, but the post-HIP hardness was nearly uniform.

Acknowledgements

Penn Rawn

I would like to thank my lab partners Haijian Yang and Jill Stinehart for their help. Haijian provided the SEM images. Jill Stinehart helped confirm that the image analysis was repeatable. I would also like to thank my advisor, Dr. Le Zhou, for supporting and guiding me through these past two years. I would also like to thank the members of my defense committee, Dr. John Moore and Dr. Ray Fournelle, for taking the time to evaluate this thesis. Finally, I would like to thank my family always encouraging me.

Table of Contents

List of Tables

List of Figures

1. Introduction

Additive manufacturing (AM) is the process of building parts by adding material rather than materials removal. It is a net shape forming method. For metals, AM is largely restricted to either laser-based or electron beam-based technologies.

Of the various possible additive manufacturing processes, laser powder bed fusion (LPBF) is the most common. To perform LPBF, it is first necessary to create a 3D computer model of the object to be built. Another computer program, the slicer, divides the model into 2D slices and feeds that information to the printer.

Powder is then deposited and scraped smoothly to form a specified layered thickness. Finally, a laser scans the powder in a prescribed pattern to create layer according to the current slice. More powder is deposited and the process is repeated until the entire object is created [1, 2].

Thermal stress, porosity, surface roughness, and anisotropy are common issues that need to be addressed with LPBF. Thermal stress can cause cracking, warping, and dimensional instability. Thermal stress is the result of the rapid heating/cooling cycles inherent in laser processes. Lasers rapidly heat small areas to high temperatures, causing a high thermal gradient. The metal then cools quickly. The molten metal is seated on a much cooler, solid substrate which prevents free contraction when the melt solidifies, leading to thermal stress. In traditional single-pass welding, the tensile thermal stresses act perpendicularly to the melt pool boundary [3]. Applying this concept to a single layer LPBF build with overlapping scan lines, the stress profile quickly becomes more complicated, but it is clear that the stresses will eventually concentrate at the specimen's

edges parallel to the scan line. Changing the scan direction between layers helps to balance the thermal stresses.

1.1. Background

Out of the several problems related to additive manufacturing, porosity is one of the most significant. Pores are formed by one of two mechanisms, depending on the energy input [1]. At lower energy inputs, powders do not always melt completely, or the melt pools may solidify before converging. Pores formed by this mechanism are often called lack of fusion voids (also called faceted voids).

Alternatively, gas pores form at higher energy inputs when gas is entrapped within the melt pools. The cooling rate is extremely high, so the gas is unable to escape before freezing. Gas pores are nearly spherical and typically smaller than lack of fusion voids. Lack of fusion voids are more angular than gas pores and may be very large, as will be seen in the Results section. Another defect, related to gas porosity, is called ”keyholing”. During keyholing, alloying elements vaporize which drives the melt pool deeper into the alloy. When unstable keyholes collapse, gas may be trapped and form porosity deep within the melt pool [1].

Broadly speaking, parametric optimization and post-processing are the two methods used for reducing the number of defects and thus improving the mechanical properties. What has often been done by researchers is to use manufacturer-set parameters to limit the as-built porosity and then use post-processing to further improve the properties. During parametric studies, researchers vary at least one of the four main parameters that influence the energy input [2, 4]. These four parameters are typically

combined into the single-value global energy density (GED), defined as

$$GED = \frac{P}{v*h*t} \quad (1)$$

In equation 1, P stands for laser power, v is the scanning speed, h is the hatch spacing, and t is the layer thickness. Even though four parameters combined determine the energy input, each needs to be studied independently. Two identical components built at the same energy input may still have different properties. Thijs *et al.* [4] studied the effect of changing velocity and hatch spacing while holding other parameters constant. They found that scan speed affects melt pool stability, grain alignment, and porosity when all other parameters were held constant. When changing only the hatch spacing, they found that overly large values resulted in forming large pores in between scan lines with consistent spacing. Note that they used a zig-zag scan strategy rather than a rotating scan strategy. Rotating the scan direction and remelting will help reduce porosity, but the initial defects are likely similar to what was reported [4]. For illustration, consider the hatch spacing, or distance between scan lines. Considering how energy varies across scan lines, porosity will be distributed differently along the scan line than between scan lines. Even if the other parameters are adjusted to maintain the GED, porosity will be distributed differently.

Ideal lasers have a Gaussian intensity distribution and quickly lose energy at the circumference of the beam [3]. Energy is concentrated along the center of the scan lines. If the hatch spacing is increased, and the travel speed has to be decreased proportionally to maintain the GED, then energy will be concentrated for a longer time over a smaller percentage of the surface. Alternatively, if the scan speed is kept constant and the power is increased to maintain the GED, then more power will be concentrated over a smaller

area than with the lower hatch spacing. Figure 1 illustrates the proposed relationship between energy concentration, scan line location, and porosity formation.

Continuing with the idea of energy concentration influencing porosity, consider a very large hatch spacing, and very high laser power. Spherical (gas) pores will be more likely to form along the scan lines. Faceted voids are more likely to form between the scan lines [5].

It is also easy to understand the importance of layer thickness. A mechanically sound AM component requires complete bonding between layers. With a larger layer thickness, fewer layers are remelted and there will be poor bonding or delamination [6]. On the other hand, each time a layer is remelted there is a chance for gas porosity to form. With excessive remelting in very thin layers, thermal stresses accumulate with each remelt which can lead to distortion and cracking [1]Additionally, decreasing the layer thickness increases the build time, which is not desirable.

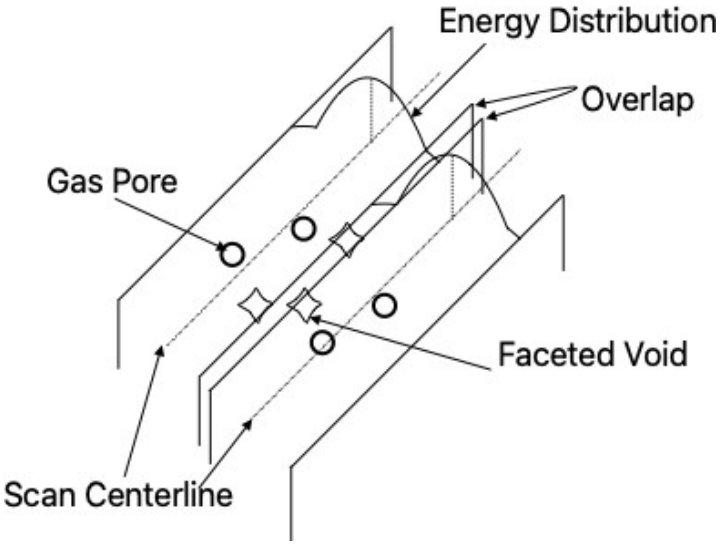

Figure 1 Drawing demonstrating energy distribution and porosity formation based on scan track location.

Laser characteristics including wavelength, spot size, and intensity also influence the results of LPBF [7]. While these characteristics are strongly interrelated, the wavelength is the most fundamental and sets practical limits on the others. The physics of diffraction limits the minimum spot size such that it decreases proportionally with wavelength [8]. The spot size, in turn, controls the upper limit for laser intensity (the power per unit area; here the intensity is reflected by the GED). Lower spot sizes allow higher intensities to be reached and therefore allow for a higher energy input. Metals also generally absorb more energy from lasers with shorter wavelengths [8]. The lower the wavelength, the smaller the minimum spot size, the higher the possible intensity and the more efficiently the metal absorbs the lasers energy.

Aside from material absorptivity and laser characteristics, the fact that LPBF is powder-based also influences the efficiency of LPBF [6, 8]. When a laser hits a solid substrate, it can either be reflected, absorbed, or transmitted. With a powder bed, however, the laser can also penetrate into the thickness of the bed and get scattered by the powder particles instead of simply being reflected [8]. The scattered beam is therefore exposed to more surfaces, and so a higher percentage of energy is absorbed than would be in dense solid [6].

Emminghaus *et al.* [9] tested two different powders at five different levels of laser power, travel speed, and hatch spacing for Ti-6Al-4V. After statistical analysis, they found that each parameter contributed to porosity. According to their regression the two-factor interactions and single-factor quadratic terms were significant. The laser power/travel speed interaction was identified as being the most influential factor affecting porosity for a given powder and layer thickness.

While holding the GED at 65 J/mm^3 and using a layer thickness of 25 μm, Pal *et al.* [10] evaluated the effect of changing power, hatch spacing, and travel speed on Ti-6Al-4V. In the first of two phases, they changed the power and speed while holding hatch spacing at 77 μm.In this first phase the density varied from 99% at 85W, 680 mm/s to 99.77% at 55W, 44 mm/s. In the second phase holding power constant at 65W, specimens fabricated with hatch spacings lower than 71 μm had densities of 99.8% or higher. Specimens built with hatch spacing greater than 77 μm had consistently lower relative densities near 99.7%. The variation observed in these results justifies the need to better understand how each parameter affects the final product, and not just the total energy input.

1.2. Hot Isostatic Pressing

Hot isostatic pressing, or HIP, is a commonly used post-processing technique to reduce porosity. Outside of the additive manufacturing industry, it is commonly used in powder metallurgy, ceramic processing, and casting to remove porosity and void space. During HIP, a chamber is filled with an inert gas (typically argon, sometimes nitrogen) and heated so that a high temperature and pressure is maintained. The combination of the two causes internal voids to collapse and close.

Closing pores requires diffusion of gas through the alloy, collapse of the pore itself, and welding of the pore walls. Under HIP conditions, pores would normally be expected to close almost instantly [11]. Process gas trapped within the pores prevent full closure. Decreasing the pore size while gas remains within the pore results in an increase in internal pressure. The only way to relieve the change in pressure is for the gas to diffuse

through the metal. Gas solubility in solids increases with pressure [12], which in turn facilitates diffusion. The few smaller, spherical pores that remain may be due to the poor solubility of argon [11]. Alternatively, some of the gas may have come out of solution during cooling; gas solubility in solids is generally more dependent on pressure than temperature, though. Gas coming out of solution while still under high pressure is probably low.

While HIP is a working method, there are still limitations. For example, HIP can only work on internal defects. Interior pores can be closed because the pressure will be acting on the walls around the entire circumference. If the pore is on the exterior, then the gas will enter the pore and act on both the interior and exterior wall, preventing closure; the pressure from HIP sometimes causes exterior pores to open [5]. Gaseous porosity has been found to reform during post-HIP heat treatment [5, 13, 14, 15]. Retaining the open porosity is an issue because stresses tend to be highest on external surfaces. Fatigue life in particular is extremely sensitive to surface condition.

Another potential issue with HIP is excessive grain growth. Grain growth occurs during any heat treatment and leads to decreased yield strength [14, 16, 17]. Tammas-Williams *et al.* [13] tracked individual pores in Ti-6Al-4V after various post-HIP heat treatments found similar results. Cunningham *et al.* attempted a super-β solution treatment to refine the post-HIP microstructure. Gas porosity renucleated as expected, but the resulting pores were still smaller and less numerous than in the as-built specimens. Both studies showed that only the gaseous pores were regrown. In addition, through electron backscattering diffraction and crystal plasticity modeling, Cunningham *et al.* found that the residual stress around the regrown pores was lower than surrounding the as-built pores [14].

As an alternative to solutionizing post-HIP, some researchers have been motivated to attempt HIP at low temperature and high pressure in an attempt to limit or moderate the level of grain growth. Moran *et al.* [16] compared the microstructure after three different HIP cycles: standard 920 ˚C 100 MPa, super-beta 1050 ˚C 100 MPa, and LTHP 800 ˚C 200 MPa. They confirmed that the LTHP specimens had smaller α lathes (both length and width) and significantly longer fatigue life after the LTHP cycle.

Alegre *et al.* [17] performed an LTHP cycle at 850 ˚C and 200 MPa. In their study the post-HIP specimen had a yield strength lower than the as-built specimen but still higher than the wrought reference. In fatigue, the post-HIP specimens performed comparably to the wrought reference, demonstrating the effectiveness of the LTHP cycle. In addition, they compared their results to others published in literature and showed that specimens treated by LTHP generally perform better in high cycle fatigue.

Fatigue life is a complicated phenomenon that may be controlled either by defects or by microstructural features. Classical fracture mechanics holds that the largest defect controls failure [18, 19]. More sophisticated models attempt to correct for location and shape, with sharp defects (stress concentrations) near the surface (location under highest stress) being the most severe case. Fatigue life in AM metals is often modeled according to the Murakami model, which relates the fatigue strength to the critical defect size [16, 20, 21]. In the absence of a critically sized defect, the failure mechanism transitions to microstructure-controlled mechanisms related to the orientation of the hcp (hexagonal close pack) basal plane [16]. As heat treatment temperature increases, the β phase and $\beta - \alpha$interface also become more important.

1.1. Ti-6Al-4V

Ti-6Al-4V is a dual-phase titanium alloy consisting of hcp α and bcc (body centered cubic) β phases [4]. When cooled from the molten state, the alloy initially solidifies in the β phase. The next transformation depends on the cooling rate. If the cooling rate is slow, most of the β will transform into α. If the cooling rate is very high, it will transform into the martensite phase. Under LPBF conditions, hcp α' martensite forms [22]. Since α' and α are both hcp, distinguishing the two by spectroscopy is difficult. Under the microscope, the martensitic phase has a distinct acicular or needle-like structure, whereas the equilibrium $\alpha - \beta$ structure that forms after slow cooling is equiaxed [22]. Heating above the martensite transformation temperature will result in the formation of near-equilibrium $\alpha - \beta$ lamellar layers.

Martensitic Ti-6Al-4V tends to be brittle, with high strength and elongation less than 10% at fracture [22]. Along with the defect density, the non-equilibrium microstructure is another motivation for post-processing LPBF specimens. A variety of microstructures may form after heat treatment depending on temperature and time [20, 22]. The possible microstructure ranges from lamellar at low heat treatment to bimodal microstructures as the β transus is approached. Mixtures of lamellar and bimodal structures form at moderate heat treatment temperatures.

Leuders*et al.*[23], comparing heat treatment at 800 ˚C and 1050 ˚C to HIP at 920 ˚C and 100 bar, found that at lower temperatures the microstructure transformed into α without noticeable coarsening. At 920 ˚C, small amounts of β were found with moderate

coarsening. It was only at the supertransus 1050 ˚C that significant coarsening and changes in grain morphology were observed. Qu *et al.* [20] performed a similar study over a wider temperature range. Specimens were stress relieved LPBF fabricated Ti-6Al-4V at 550 ˚C followed by annealing at nine different temperatures from 600 ˚C to 1050 ˚C. After annealing they reported the difference in microstructure, hardness, and fatigue life at 650 MPa. They found that while martensite decomposition began even after stress relieving without annealing, grain coarsening remained insignificant at 600 ˚C and 700 ˚C. In addition, the α lathes maintained alignment with the initial α' structures below 950 ˚C. As the annealing temperature approached the β transus (1050 ˚C), more α transforms into β and the original grain orientation begins to disappear.

2. Methodology

2.1. Parametric Study

Two builds of Ti-6Al-4V were made on an EOS M100 LPBF machine. The EOS M100 uses a circular 100 mm diameter build plate. Powder is dispensed from a hopper located directly within the build chamber. A set of carbon fiber brushes was used to level the powder bed between scans. Materialise Magics software was used to generate the 3D models and slice them into files that could be read by the printer. Labels corresponding to the build parameters were printed directly on the specimens. In addition to alternating the scan axis between x and y, the scan axes were rotated 67 ˚C between layers to balance the thermal stresses. The default autogenerated supports provided by Magics were built between the specimens and the build plate. Specimens were located on the build plate so that the cubes built with the highest GED were near the vacuum to prevent spatter and any offgassing from contaminating the other cubes. Those built at the lowest GED were located at the far side of the plate from the scraper to prevent them from crashing into the others in the event of separation from the plate.

The first build was built with a layer thickness of 20 μm. Eight specimens (Figure 2 were built by varying the parameters of laser power, scan speed, and hatch spacing according to a two-level factorial experimental design. A ninth control specimen was built using the machine default parameters. Table 1 shows the printing parameters for each specimen. One of the cubes on the plate has a large split about halfway through the specimen. During the build, the hopper ran out of powder and had to be refilled. Because the hopper is located directly in the build chamber, the build had to be stopped and the atmosphere broken to refill. Oxygen again had to be purged from the chamber

and the argon atmosphere rebuilt before the build could resume. The specimens cooled during the refill time, and the cube with the lowest energy density experienced poor fusion during the following layer. However, only the area within a few layers of the center should be affected by this issue and the effect on average porosity is expected to be negligible. The area near the center was avoided during microscopy.

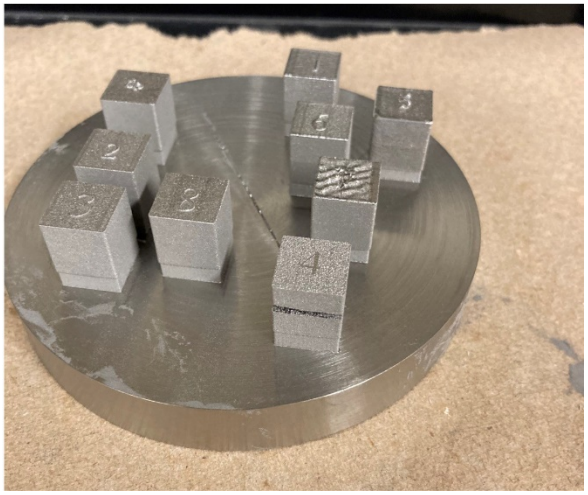

Figure 2 Cubes built using a layer thickness of 20 μm layer thickness on build plate.

Table 1 Process parameters for layer thickness of 20 μm

Specimen	Laser Power (W)	Travel Speed (mm/s)	Hatch Spacing (mm)	GED (J/mm^3)
A1	70	700	0.04	125
A2	70	700	0.08	62.5
A3	70	1300	0.04	67
A4	70	1300	0.08	34
A5	130	700	0.04	232
A6	130	700	0.08	116
A7	130	1300	0.04	125
A8	130	1300	0.08	63
Op	100	1400	0.06	60

A second build was made utilizing a 40 μm layer thickness. Of the thirteen specimens listed in Table 2, eight were made according to factorial experimental design (DOE specimens). Five additional (Aux specimens) specimens were built at more moderate laser power and lower scan speed to try capturing the effects of a wider GED range for the higher layer thickness. Table 2 contains the build parameters. On these specimens, the labels did not print and the specimens were identified based on their position on the build plate. A vibro peen was used to properly label the specimens before they were removed from the build plate.

Table 2 Process parameters for layer thickness of 40 μm

Specimen	Laser Power (W)	Travel Speed (mm/s)	Hatch Spacing (mm)	GED (J/mm^3)
B1	120	600	0.06	83
B2	120	600	0.1	50
B3	120	1200	0.06	42
B4	120	1200	0.1	25
B5	170	600	0.06	118
B6	170	600	0.1	71
B7	170	1200	0.06	59
B8	170	1200	0.1	35
B9	150	600	0.06	104
B10	150	600	0.1	63
B11	150	1200	0.06	52
B12	170	400	0.06	177
B13	170	400	0.1	106

2.2. HIP Procedure

Cubes were removed from the build plate by the Marquette University DLC machine shop. A low speed saw using oil coolant was then used to section the as-built

cubes so that the porosity and microstructure parallel to the build direction could be viewed. Two sections were mounted from each cube in the as-built condition: a z-section (parallel to the build direction) and a x-y cross-section. The remaining portion of each cube was then subjected to the LTHP HIP cycle for two hours. After HIP, specimens were mounted so that the post-processed z-section could be analyzed.

An IPS Eagle HIP system was used to perform the post-treatment. During the HIP cycle, oxygen was first evacuated from the chamber by building a vacuum of 26.7 Pa. After the vacuum was built, two purge cycles where the chamber was filled with argon to 0.7 MPa and vented. After the purging, the chamber was prefilled to 7 MPa and the LTHP cycle was started. The LTHP cycle used a temperature of 850 ˚C and 200 MPa.

Figure 3 plots the real-time pressure and temperature data as measured during the HIP cycle. Ignoring some noise early in the cycle, temperature is observed to rise linearly from room temperature to the set temperature at a rate of 10 ˚C/s. The jumps in the pressure plot correspond to times when the gas compressor was running. Temperature control was fully automatic, while the compressor had to be run in semi-manual mode to conserve argon.

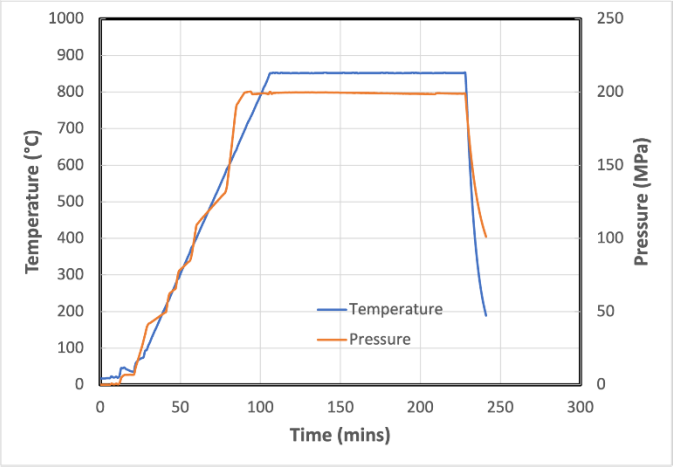

Figure 3 Temperature and pressure measured during LTHP HIP cycle.

Since gas pressure within an enclosed space naturally increases with temperature, the compressor has a separate setpoint from the final pressure setpoint. Initially, the compressor ran to a setpoint of 70 MPa. Pressure was then allowed to increase naturally with temperature. However, since the actual pressure increases more slowly than may be necessary for to reach the required pressure before the temperature ramp increases. The software also reads out a current setpoint indicating what the pressure should be at a given time to reach the final pressure. Whenever the pressure reading fell below the current setpoint, the compressor was turned on again for approximately two minutes.

After HIP, the specimens were allowed to cool to room temperature before beginning the venting procedure. During venting, the furnace was manually controlled to keep the temperature between 80˚C and 120 ˚C. Upon completion of venting, the chamber was again allowed to cool to near room temperature before removal.

2.3. Porosity and Microstructure Evaluation

Mounted sections were ground down to 1200 grit using SiC paper, and then further polished to 0.05 μm using alumina powder. Ten random micrographs of the unetched surfaces were then taken to analyze pore shape, size, and overall density. All images were taken of the surface perpendicular to the build direction. For the purpose of this thesis, "density" refers to the relative density:

$$\text{Relative density} = 1 - \text{porosity} \tag{2}$$

Porosity was measured via area analysis using ImageJ analysis software after setting a threshold and converting the color image to a black and white image. Multiple shape factors are available to choose from, but the aspect ratio was chosen because it is the most commonly used. The aspect ratio is calculated by drawing an ellipse around the features and then dividing the major axis by the minor axis; the higher the aspect ratio, the further it deviates from a circle. Pore size was measured by averaging the longest and narrowest distances between two non-adjacent points on the perimeter.

After taking pictures for analysis, the specimens were etched using Kroll's Reagent (4.7% nitric acid, 1.9% hydrofluoric acid, remainder water) to reveal the microstructure and melt pools. Kroll's reagent is a commonly used etchant for revealing the microstructure of dual-phase titanium alloys.

Microhardness measurements were performed using a Vicker's diamond indenter with a 1000 gf load and dwell time of 20 seconds. Five measurements were made on each specimen. Diagonals were measured using the tester's built-in micrometer. The hardness was calculated using

$$hv = 1.8544 * \frac{f}{d^2} \tag{3}$$

where f is the load in kgf and d is the average diagonal length in mm.

3. Results

3.1. Porosity

Figure 4 represents the porosity in the as-built and post-HIP condition for both the 20 and 40 μm prints. Points above the diagonal line represent specimens that increased in density after HIP. Points below the line indicate a decrease in density resulting from the HIP cycle. From these plots, it is clear that in most cases HIP is beneficial for removing defects in LPBF Ti-6Al-4V.

Figure 5 plots the as-built porosity compared to the global energy density. As the GED increases, the overall density increases to a maximum and then decreases again as keyholing occurs. The data behaves as expected from the literature.

3.1.1. 20 μm Print

Porosity of the as-printed specimens is shown in Figure 6. One of the most striking observations from these images is the size and sharpness of pores in the fourth image, the one built at the lowest GED. A wide variety of build parameters was used, which resulted in the varied porosity results.

Table 3 lists the as-built and post-HIP porosity measurements along with the GED. Shape is measured as the aspect ratio. To find the aspect ratio, an ellipse is drawn around each pore, and the major axis is then divided by the minor axis.

Values near one represent a circle, and large numbers indicate a nearly linear defect. While there is a wide variation in pore size, the aspect ratio remained with the narrow range of near 1.5 to 1.9. Size and shape distributions for all 20 μm specimens may be found in Appendix A

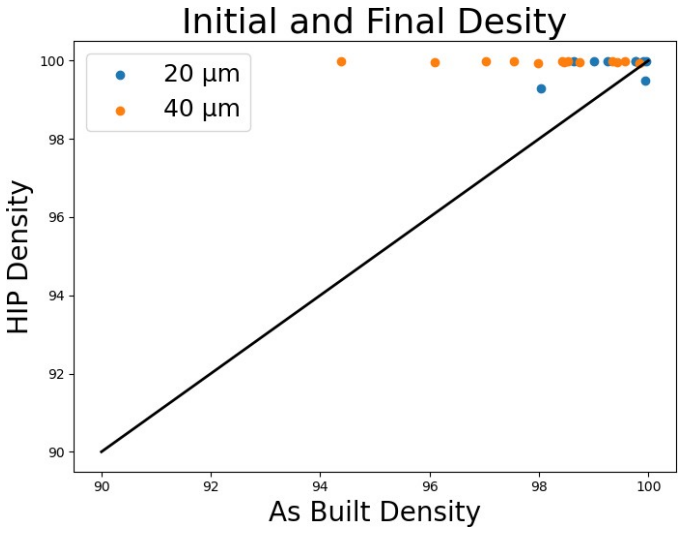

(a)

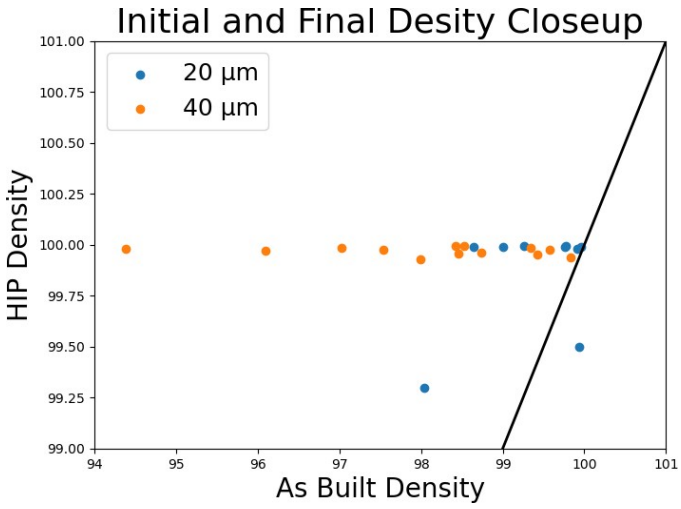

(b)

Figure 4 a) Density before and after HIP. b) Close up data

In the post-HIP condition, porosity consistently decreased for all but one specimen. Specimen B7 had an anomalous pore. The outlier was left in because even though it was the only notable pore, it was still about 2 mm from either of the nearest edges. With that one exception, the images show a dramatic porosity decrease after the LTHP cycle. Images demonstrating the effectiveness of the LTHP cycle are available in

Figure 7.

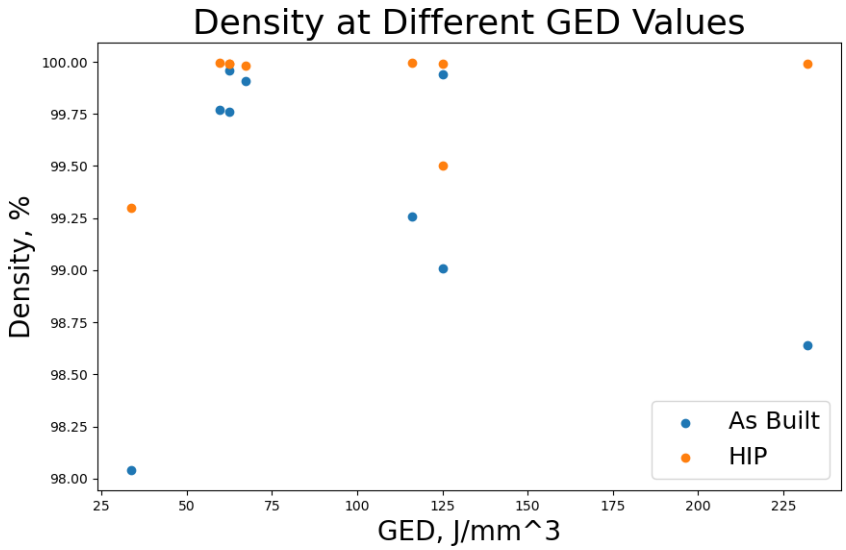

Figure 5 Relationship between initial porosity and GED

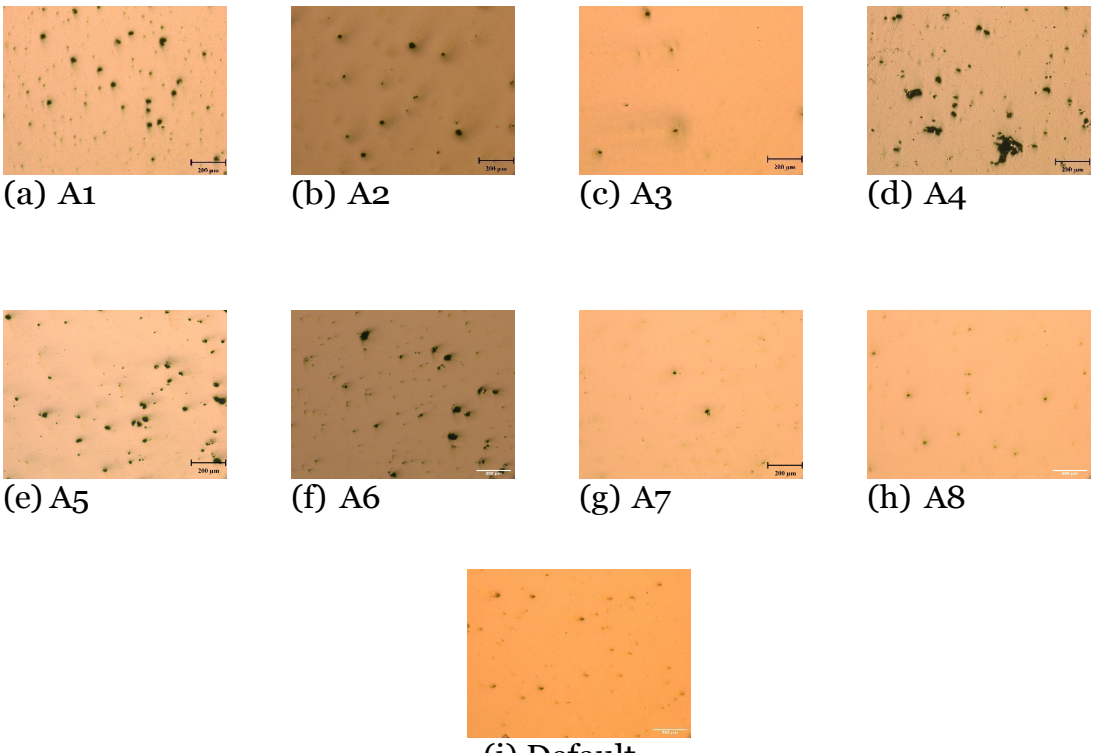

Figure 6 Representative porosity of 20 μm print in the as-built condition

3.1.2. 40 μm Print

The 40 *μm* print had an even wider variation in the as-built porosity (Figure 8). In this print, there was a wider variation in porosity, even though the GED range was more restricted. Figure 9 shows that porosity was still effectively removed. Table 4 lists the porosity before and after HIP. Size and shape distributions for the 40 *μm* build are available in Appendix B.

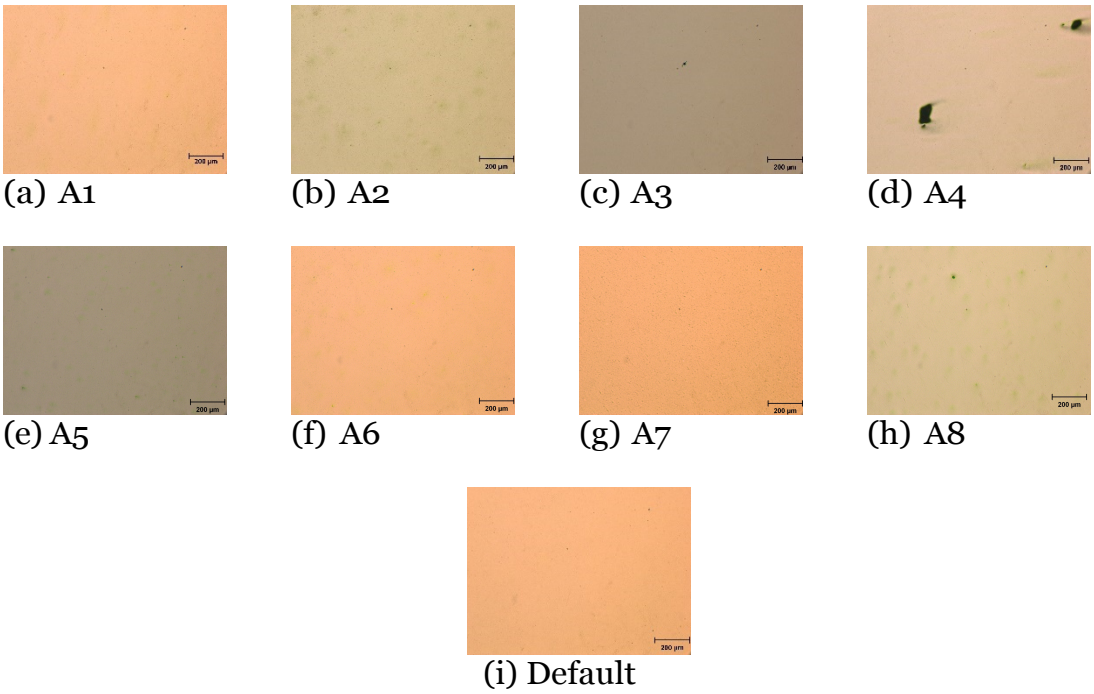

(a) A1 (b) A2 (c) A3 (d) A4

(e) A5 (f) A6 (g) A7 (h) A8

(i) Default

Figure 7 Representative porosity of 20 *μm* print in the post-HIP condition

Table 3 As-built density and pore characteristics of the 20 μm print

Specimen	GED (J/mm^3)	AB Density (%)	AB Pore Size (μm)	AB Aspect Ratio
A1	125	99	9.78	1.59
A2	63	99.8	14.7	1.48
A3	67	99.9	11.7	1.86
A4	34	98	8.77	1.64
A5	232	98.6	14.5	1.67
A6	116	99.3	8.86	1.61
A7	125	99.9	4.51	1.54
A8	63	100	5.34	1.53
Default	60	100	4.90	1.81

Table 4 As-built density and pore characteristics of 40 μm print

Specimen	GED (J/mm^3)	AB Density (%)	AB Pore Size(μm)	AB Aspect Ratio
B1	83	98.7	21.2	1.53
B2	50	98.0	16.7	1.60
B3	42	98.5	12.9	1.61
B4	25	99.4	5.4	1.91
B5	118	94.4	18.5	1.57
B6	71	96.1	18.7	1.54
B7	59	99.8	12.3	1.55
B8	35	99.6	6.28	1.37
B9	104	97.5	13.5	1.69
B10	63	97.0	18.0	1.60
B11	52	99.4	15.8	1.68
B12	177	98.5	12.8	1.48
B13	106	98.4	11.2	1.63

3.2. Microstructure

Etched specimens reveal a microstructure consisting of acicular martensite in the as built specimens (Figure 10). Acicular α' martensite forms when the cooling rate exceeds 410 ˚C/s [24]. After HIP, however, a coarser microstructure consisting of α lathes is

formed. A few micrographs taken by scanning electron microscope are presented in Figure 11. The change in microstructure is much more pronounced in the SEM images. The long, narrow acicular phase is seen to transition to wider plate-like α lathes. The apparently random orientation of acicular structures in the as-built images correlates to the prior beta grain orientation. In the post-HIP condition, there are still changes in the orientation but the microstructure generally appears more uniform.

3.3. Microhardness

After etching, the Vicker's microhardness of all specimens was measured to assess the effect of HIP on mechanical properties. Table 5 contains the average of five measurements for the $20\mu m$ build in both the as-built and the post-HIP condition. The last column is the percent change in hardness calculated by

$$Diff = 100\% * \frac{initial - final}{initial} \quad (4)$$

Most specimens significantly decreased in hardness by up to 12.3%. The only exception was A4, which was built at a GED of $33.65\ J/mm^3$ and had a high level of faceted pores in the as-built condition.

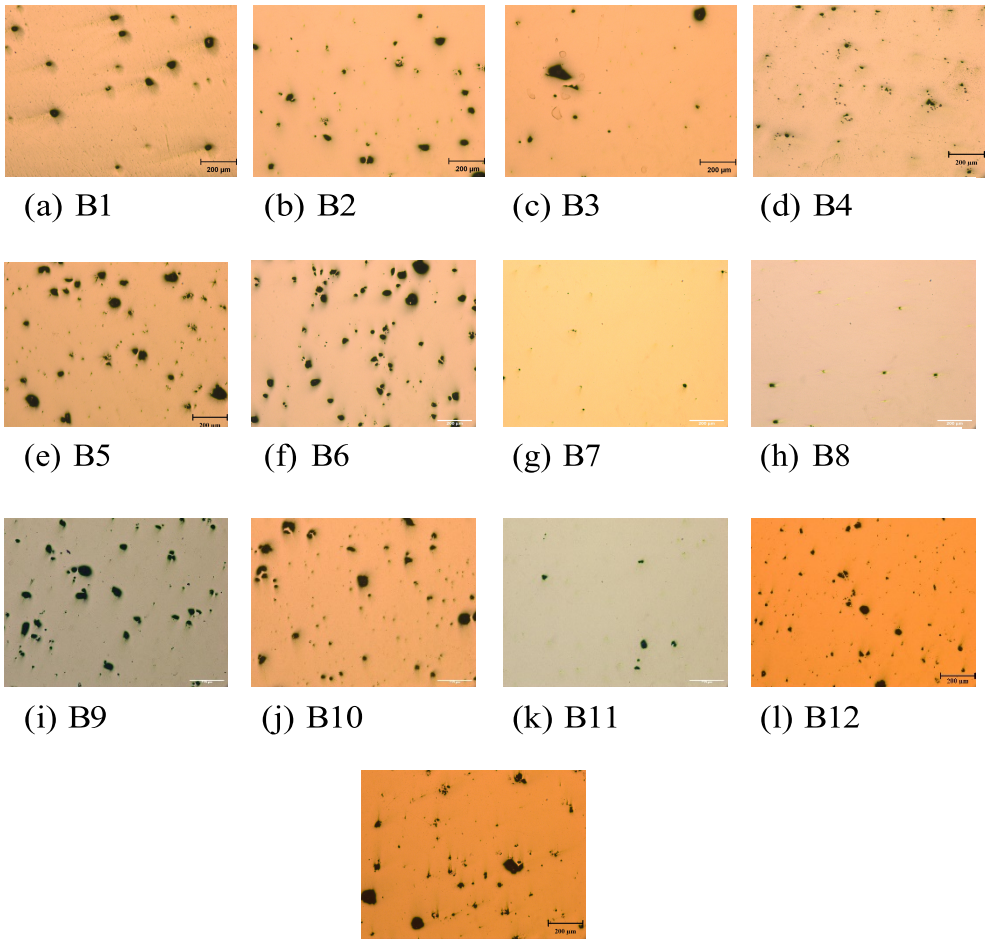

Figure 8 Representative porosity of the 40 *μm* print in the as-built condition

Table 5 Microhardness of 20 *μm* print LPBF specimens

Specimen	As-Built Hardness	Post-HIP Hardness	Difference (%)
A1	382 ±8	335 ±10	-12.3
A2	356 ±8	338 ±5	-5.6
A3	364 ±4	334 ±3	-8.2
A4	320 ±10	324 ±6	1.3
A5	341 ±20	338 ±7	-0.9
A6	356 ±31	319 ±4	-10.4
A7	364 ±10	342 ±5	-6.0
A8	373 ±6	335 ±5	-10.2
Default	374 ±3	328 ±4	-12.3

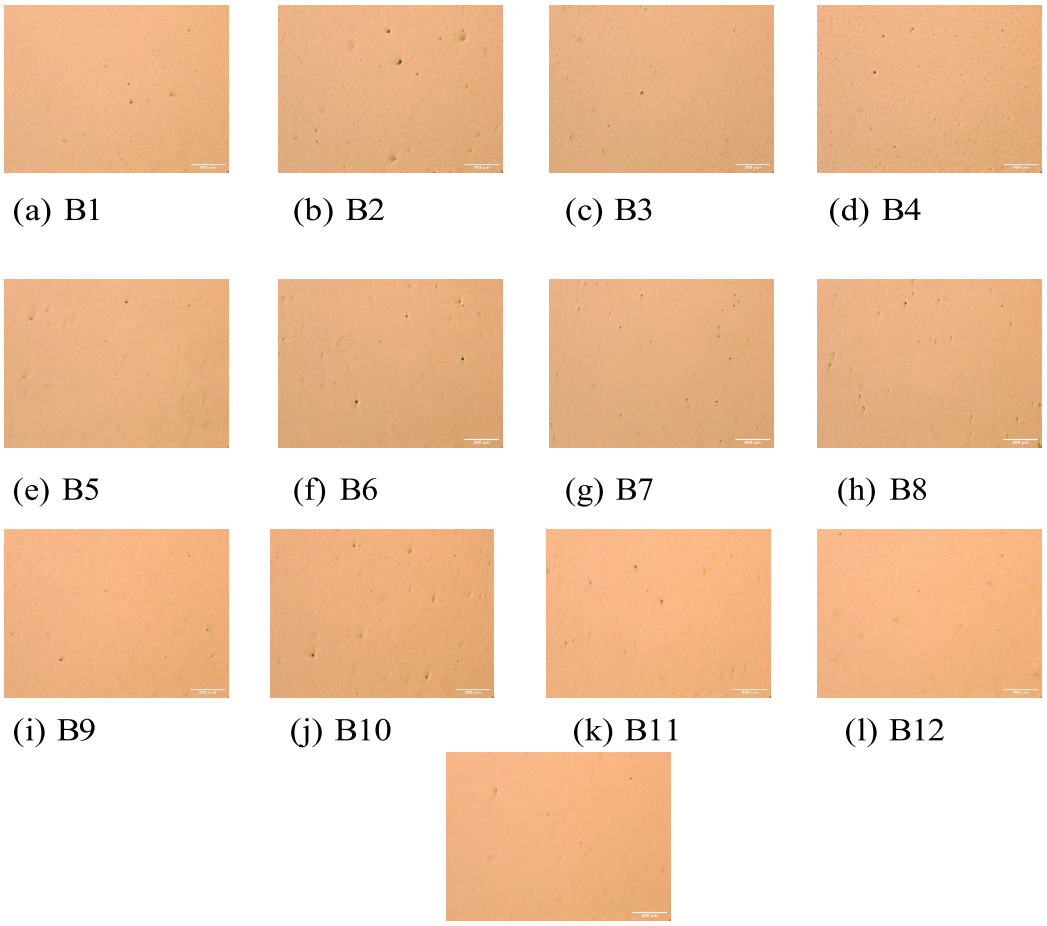

Figure 9 Representative porosity of the 40 μm print in the post-HIP condition

Table 6 lists the same information for the specimens built at 40 μm. Again, in all but one specimen the hardness decreased by up to nearly 12% after the LTHP cycle. Specimen B12, built at 177 J/mm^3, was the only specimen in this set to increase in hardness after HIP.

Figure 12 graphs the above hardness data against the GED with scale bars representing the standard deviation. Interestingly, the specimen built at 34 J/mm^3 increased in hardness after HIP, while the rest decreased. In the 40 μm build, the hardness consistently decreased after HIP.

In the as-built condition, hardness clearly increases with increasing density; however, the standard deviation does not follow the same trend. It appears that the porosity affects the mean hardness, but the variation is probably related to microstructural features. Plotting hardness (Figure 13) against the porosity reveals no overall trend relating the post-HIP hardness to porosity.

Table 6 Microhardness of 40 μm print LPBF specimens

Specimen	As-Built Hardness	Post-HIP Hardness	Difference (%)
B1	367 ±7	334 ±7	-9.0
B2	360 ±14	332 ±4	-7.8
B3	372 ±7	328 ±1	-11.8
B4	348 ±19	335 ±3	-3.7
B5	334 ±18	331 ±1	-0.9
B6	351 ±15	327 ±5	-6.8
B7	363 ±7	338 ±3	-6.9
B8	369 ±3	339 ±7	-8.1
B9	344 ±26	330 ±4	-4.1
B10	355 ±14	332 ±8	-6.5
B11	356 ±18	334 ±4	-6.2
B12	319 ±13	336 ±6	5.3
B13	344 ±13	332 ±6	-3.5

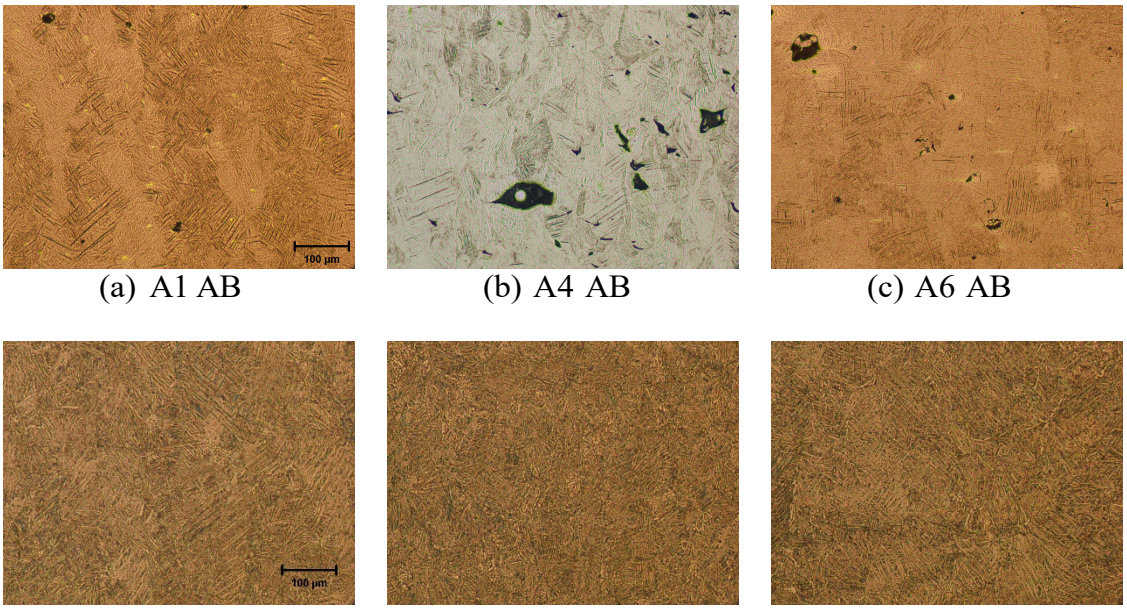

(a) A1 AB (b) A4 AB (c) A6 AB

(d) A1 HIP (e) A4 HIP (f) A6 HIP

Figure 10 Etched surfaces of 20 *µm* specimens in the as-built (top row) and post-HIP (bottom row) condition.

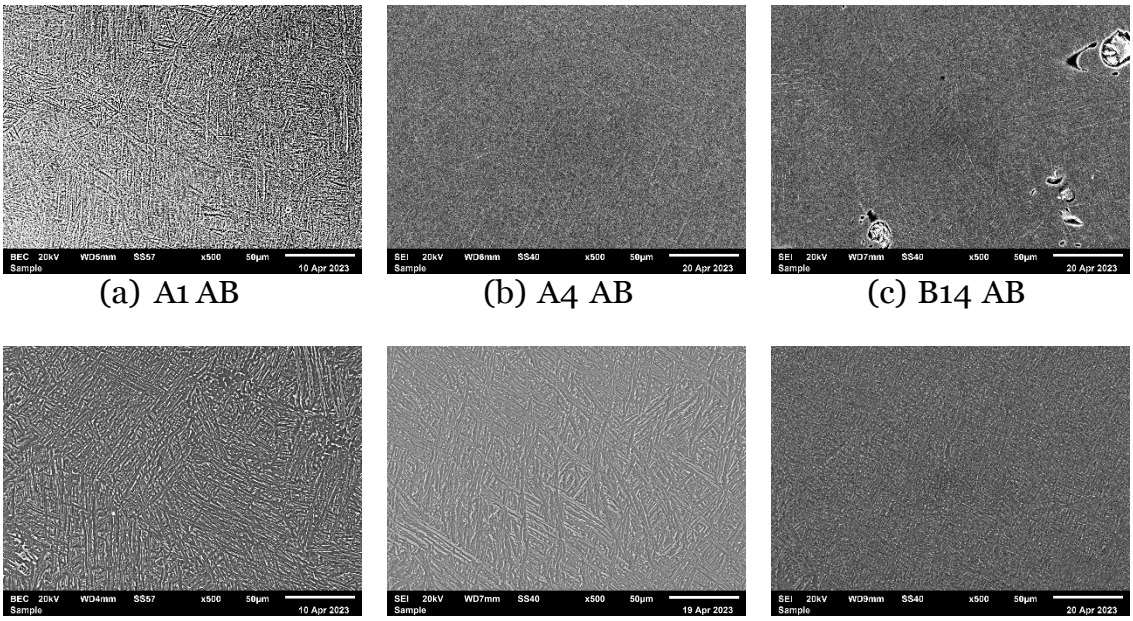

(a) A1 AB (b) A4 AB (c) B14 AB

(d) A1 HIP (e) A4 HIP (f) B14 HIP

Figure 11 SEM images of specimens in the as-built (top row) and post-HIP (bottom row) condition at 500x.

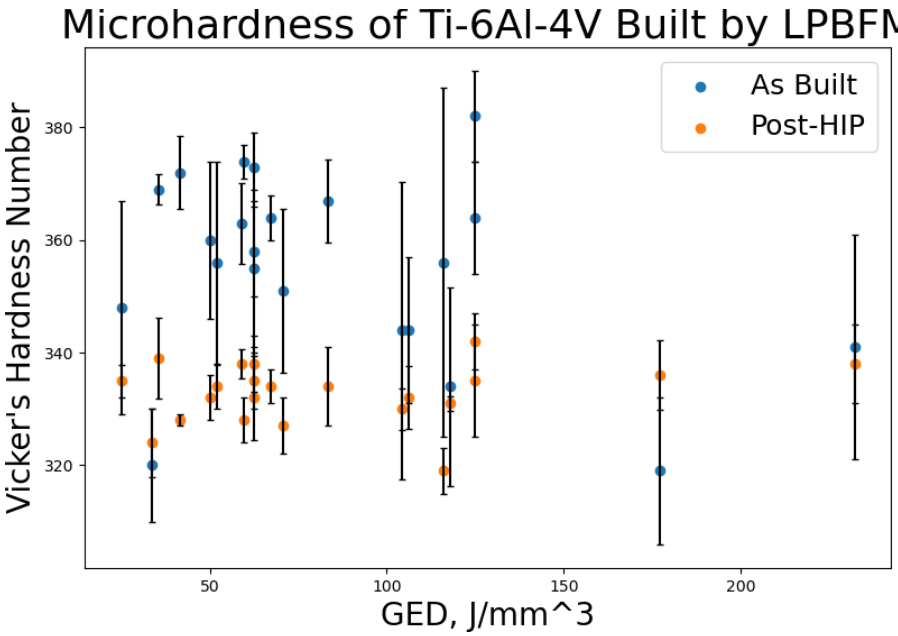

Figure 12 Vicker's Hardness number of all specimens.

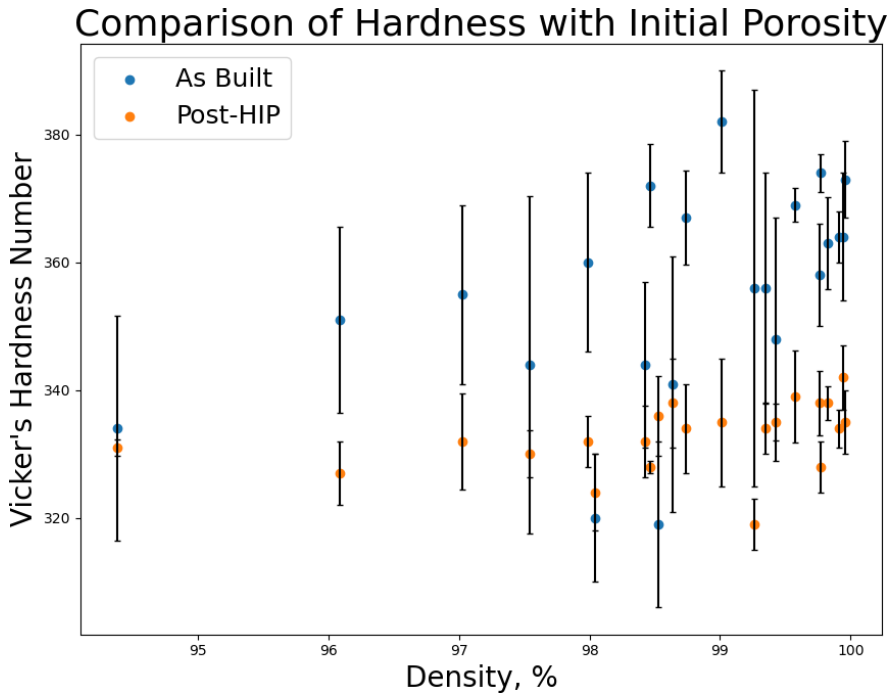

Figure 13 Relationship between initial porosity and hardness of all specimens.

4. Discussion

4.1.Porosity

When examining the overall effect of HIP on porosity, a clear trend appears in the 20 μm print, but not in the 40 μm print. With increasing GED, it is expected that the as-built porosity will increase to a peak as more complete fusion occurs, and then decrease as keyholing and gas porosity forms, as exhibited by the 20 μm print. In the 40 μm, there is no apparent trend. While the as-built porosity appears to immediately increase with increasing GED, there is a lot of scatter. In addition, specimens built at the higher layer thickness tended to be more porous in the as-built condition than those built at the lower layer thickness.

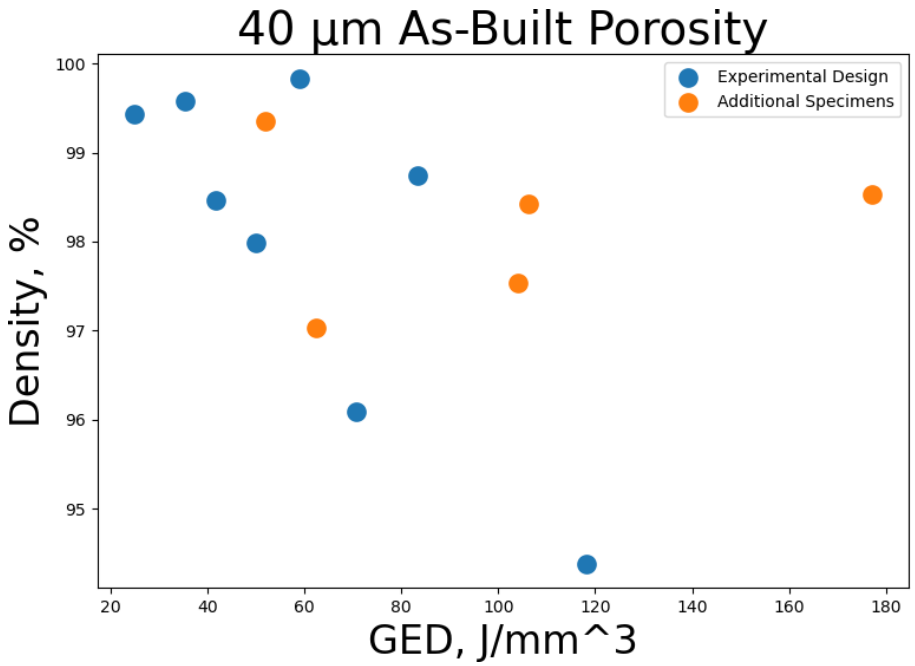

Figure 14 40 μm Print porosity separated into DOE and Aux specimens.

Figure 14 separates the porosity data for the 40 μm print into the eight DOE and five Aux specimens. Most of the scatter is due to the Aux specimens, but there are still three points for the DOE specimens that deviate from the trend.

The plot comparing the change in density to pore size requires some interpretation. Studying it, the points seem random with maybe a weak upward trend in density increase with pore size. Looking at the micrographs, however, it is the large faceted voids that remain after HIP. In the present study, all specimens still had a large number of spherical pores. The apparent, weak relationship is likely due to the fact that most of the porosity is still spherical, even at low GED values, so the specimens increased in density despite the retention of lack of fusion pores.

Figure 16 a and b, the pore size distribution before and after HIP of specimen A4, also suggests that it is only the smaller pores that are removed. A large decrease in the number of small pores occurs, while a significant number of larger pores remain. Figure 16 c and d also show that the remaining pores have generally higher aspect ratios, suggesting that it is large faceted pores that remain. It is also notable that in 3 A4 is not the specimen with the largest average aspect ratio. Even though there are several large, irregular pores, there are also smaller, rounder pores visible.

Most post-HIP specimens increased in density, clearly indicating the effectiveness of the LTHP cycle to remove porosity. Many post-HIP specimens had a porosity within less than 0.1%. Even in the most extreme cases, density increased from around 96% to over 99.9%. Although previously shown to improve mechanical properties [16, 17], there had been the question of whether the porosity had been effectively removed, because:

1. The past experiments focused on high cycle fatigue, which is more sensitive to microstructure than to defects.

2. The temperature of 850 ˚C is much lower than the standard temperature of 920 ˚C, which is closer to the β transus.

While the porosity of the 33.65 J/mm^3 specimen was largely removed by HIP, a few of the faceted voids remained. Unlike gas pores, lack of fusion pores are not likely to be under high internal pressure. Gas pores are formed due to rejected gases being unable to reach the surface before solidification which likely causes a higher internal pressure than lack of fusion pores. Some possible explanation for why the lack of fusion porosity remained post-HIP include:

1. Porosity may have been connected to the surface, allowing the HIP gas to enter into the specimen and prevent closure.
2. The internal pressure may not have been high enough to promote diffusion.
3. The faceted geometry may have prevented the pores from closing.

Considering the third explanation, HIP was initially developed for powder metallurgy to simultaneously sinter and remove porosity [11, 25]. Closing faceted pores could be analogous to the later stages of sintering: sharp angles between fused particles are rounded so that the void space becomes spherical (Figure 15). The sharp angles round off and spherical porosity forms. It is only after being rounded that the pores start to close. Post-HIP images of the specimen built at 33.65 J/mm^3 reveal the edges of the remaining pores are more rounded than in the initial surface. It may be that faceted pores need to be rounded before they can be closed. The pressure may have been high enough to promote diffusion of gas to close pores that are already rounded, but the temperature may have been too low to remove the faceted pores.

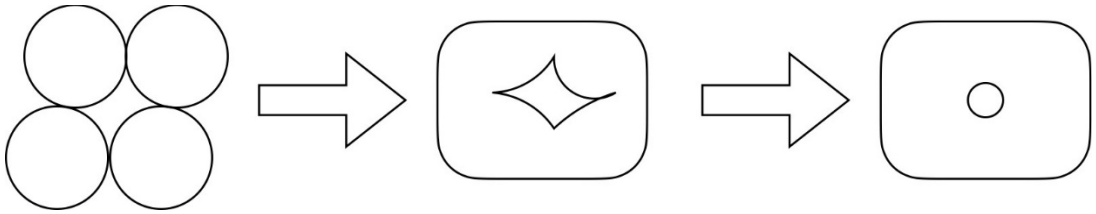

Figure 15 Stages of sintering

It was also mentioned earlier that one specimen, A7, had a single large pore remaining after HIP, even though the rest of the surface was fairly dense (Figure 18). The large pore was approximately 2 *mm* from either of the nearest edges which should normally be considered the interior. However, it was also nearly equidistant from either edge. The area of a corner is infinitesimally small and is unable to accommodate stress. It is possible that the pressure exerted by HIP could not effectively act on the pore due to how it lined up with the corner. In that case similar pores would be eliminated in round specimens but porosity along the diagonals of rectangular specimens may be less likely to recover. Alternatively, two pores may have been pushed together by the pressure. Since this is the only specimen where the phenomenon was observed it is difficult to determine the cause.

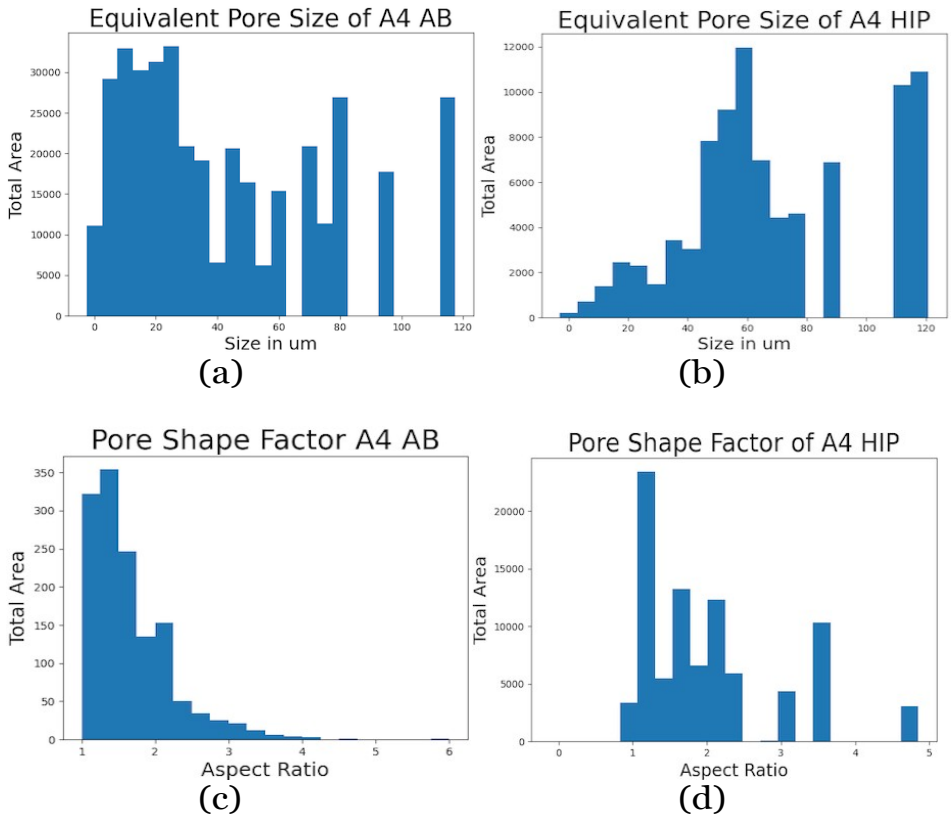

Figure 16 As-built and post-HIP pore size distributions(a,b) and aspect ratio (c,d) of specimen built at 34 J/mm^3. The y-axis is the total area of pores within each category.

Figure 17 shows similar behavior in specimen B6 built at 71 J/mm^3. In this case, almost all of the smaller pores are removed and it is primarily larger pores that remain.

Some of the difficulties in analyzing information using ImageJ come from extreme pore size values. On the one hand, in Figure 16, the number of large pores is completely dwarfed by the number of small pores measured. Even though the surface was polished well and carefully cleaned, it is difficult to determine whether the extremely small detections are actually pores, polishing media, or spots on the microscope lens. On the other hand, some of the large pores in the software's output were actually separate defects measured as one. One of the steps that ImageJ takes in calculating defects size involves

drawing ellipses around the defect. Apparently, when the defects are close enough, the ellipses overlap and the two defects are counted as a single defect. Some examples of such detections are shown in Figure 19.

Porosity was measured using a series of ten random micrographs, so that only a sample of the surface was analyzed. In addition, the analysis treats porosity as being 2D but pores are 3D features. In specimens built using high GED values especially, voids may extend deep below the surface due to keyholing [26].

4.2. Microhardness

With two exceptions, hardness decreases after the LTHP cycle. Prior research [16, 17], however, found that fatigue properties improved after LTHP. Normally hardness is expected to reflect the mechanical properties, with higher hardness indicating higher tensile strength and fatigue strength. Qu *et al.* [20]performed ten different heat treatments and found that the condition giving the lowest hardness actually gave the highest high cycle fatigue life. Fatigue is highly defect sensitive, while yield strength and tensile strength are largely controlled by microstructure and work history. Brot *et al.* built specimens at $P = 275\ W$, $v = 1100\ mm/s$, $h = 120\ \mu m$, and $t = 30\ \mu m$, then performed HIP at 920 ˚C and 2000 bar for 2 hr. Their post-HIP hardness of 368 HV [27] was higher.

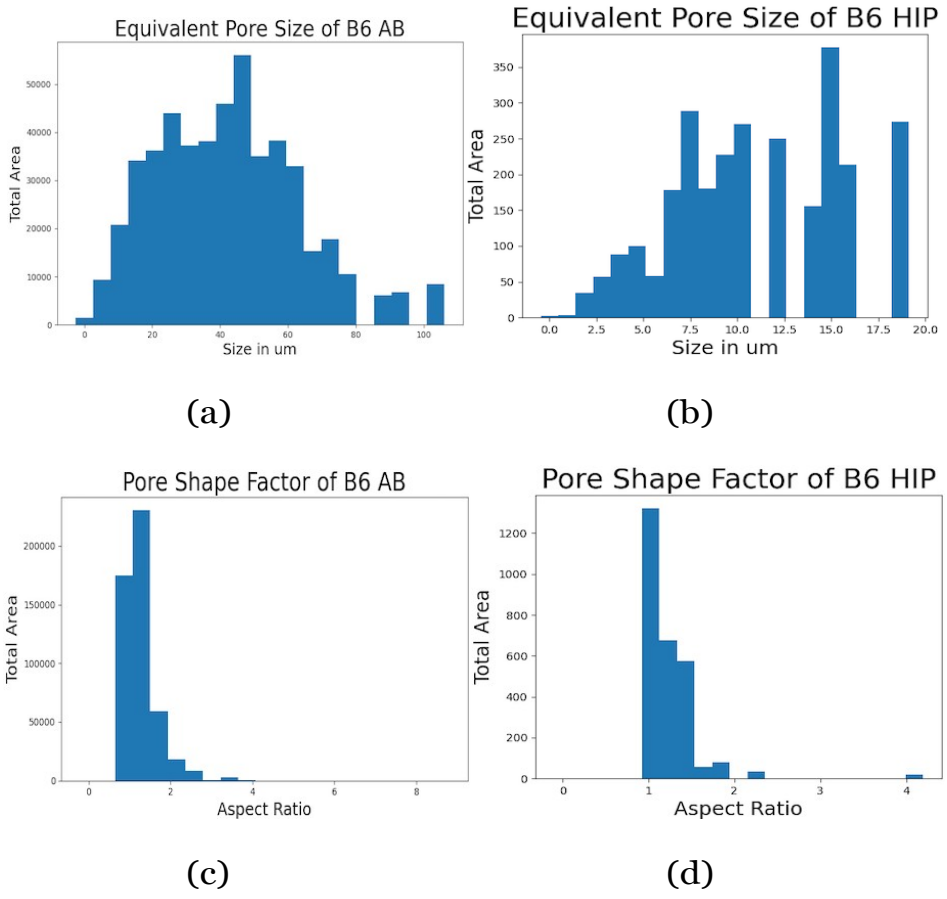

Figure 17 As-built and post-HIP pore size distributions(a,b) and aspect ratio (c,d) of specimen built at 71 J/mm^3. The y-axis is the total area of pores within each category.

While performing the hardness tests, it was immediately clear that there was more variation in the as-built specimens than in the post-HIP ones. Initially the disparity was attributed to the porosity. Plotting the hardness against density, however, revealed that the specimens with highest variation in hardness were not the most porous. In fact, both the 40 μm print and 20 μm mprint gave the highest standard deviation near middle levels of porosity. This seems to suggest that microstructural inhomogeneities contributed more to the scatter than the defects.

The same complex thermal histories and laser-melt pool interactions that cause defect generation lead to an inhomogeneous microstructure.

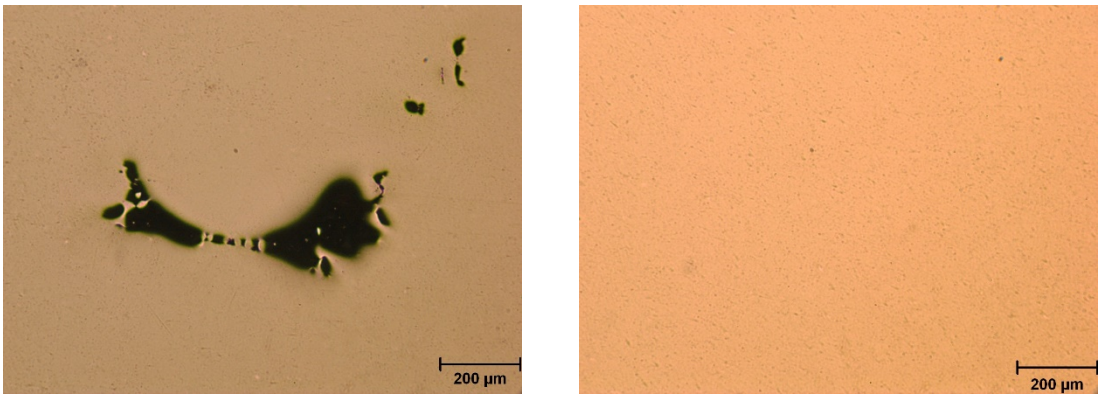

(a) (b)

Figure 18 (a) Single large pore and (b) representative image of specimen built at 125 J/mm^3 post-HIP

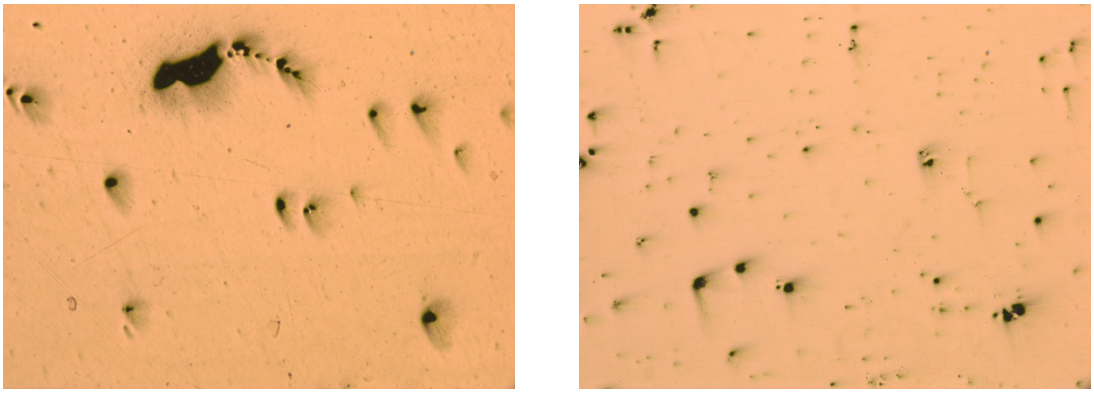

(a) A5 (b) A6

Figure 19 Examples of separate pores treated as a single pore in analysis.

While only five indents were taken on each specimen, two patterns emerge from the analysis. First, consistently on all as-built specimens, indents taken on or near the top layer (the last layer printed) had a lower hardness than interior indents. Next,

indents taken in locations where the microstructure alignment differed from the surrounding matrix had some of the lowest hardness values, as demonstrated in Figure 20. This region had a hardness of 291, as opposed to the mean value of 344. The observation of the importance of microstructural inhomogeneities is consistent with the inferences based on error bars.

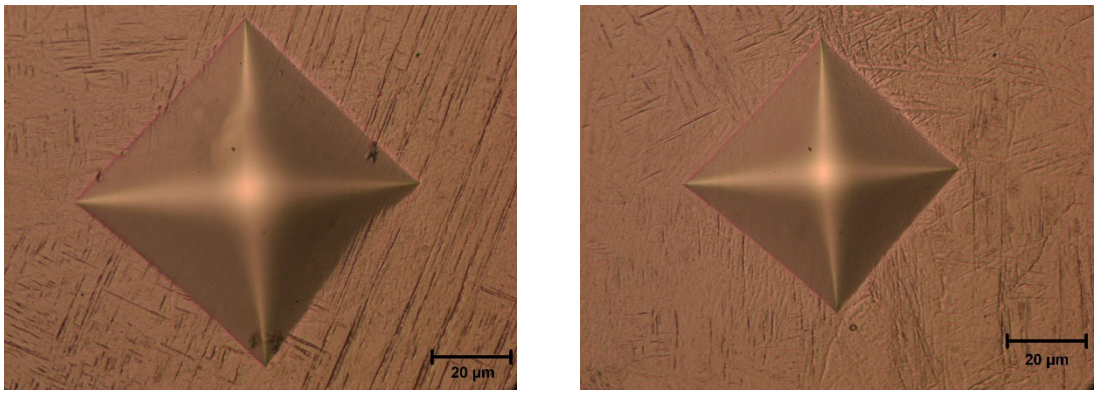

(a) (b)

Figure 20 Hardness indent in area with misaligned grains.

The main goal of the LTHP cycle is to remove defects without excessive grain growth. While the microstructure remains fairly fine, as visible in the micrographs, the microhardness measurements clearly show that material softens after HIP. The LTHP cycle temperature is much lower than that of traditional HIP, but is still high above the martensite transformation temperature (decomposition begins at about 400°C [28]). Complete martensitic decomposition occurs at between 600°C and 700°C [29] The microstructure is actually transforming from acicular martensite into a similar-looking α – β lamellar structure. Ahmed and Rack [24] claim that decomposition begins at 525°C.

5. Summary

A parametric study was performed to evaluate the effect of GED on as-built porosity and hardness. A clear trend was visible in the 20 μm print where the density reached a peak in the range of 60 to 70 J/mm^3 and decreased as the GED deviated from that range. The 40 μm print porosity appeared to follow two different trends. In the range of 25 to 100 J/mm^3, there is an approximately parabolic trend in microhardness with GED with a peak again at around 60 - 70 J/mm^3. Above 100 J/mm^3, the trend changes and the microhardness begin to increase again. The mean as-built hardness generally increased with density, but the standard deviation appears to have been controlled by microstructural features.

Specimens were post-processed to evaluate how well the LTHP HIP cycle could remove porosity. Even though there are some anomalies, the LTHP cycle consistently removed most pores. The remaining porosity consisted of primarily large, faceted voids with a few very small spherical pores also remaining. The post-HIP hardness remained in the area of 320 to 340 HV, and appeared to be mostly independent of initial porosity.

6. Future Work

The primary goal of the LTHP cycle is to avoid excessive grain coarsening. While the change in grain size appears moderate from observing the micrographs, the as-built and post-HIP grain size should be quantified for comparison. It would also be helpful to perform more microhardness tests to further evaluate the relationship with microstructural features.

Some of the 40 μm build specimens did not follow the expected porosity trend. Specifically, the low GED specimen did not have the high level of porosity that was expected. The graph relating porosity to GED also had no clear trend. It may be worth doing a repeat of the 40μm build to confirm the presented data is accurate.

One issue with the presented data is that it treats pores as 2D features when they are actually 3D. It would be beneficial to print coupons for x-ray microtomography (micro-CT) alongside the fatigue testing specimens. Using micro-CT allows 3D images of the interior to be generated so that a complete view of the porosity can be viewed. Mainly, the porosity can be measured as a volume percentage and the penetration depth can be observed.

Low cycle fatigue testing is the next logical step. At the time of writing, research into the LTHP post-treatment has focused on high cycle fatigue and tensile properties. Low cycle fatigue testing is generally strain-controlled testing with strains entering the plastic domain. Insight into the evolution of plastic deformation under cyclic loading conditions can be gathered from low cycle fatigue data but is not available from high cycle fatigue tests. Fatigue tests are time consuming, so the list of parameters presented should be narrowed down before building.

After the LTHP cycle, all specimens approached full density. There is still a quest of whether specimens built at none-optimal parameters have the same or similar fatigue behavior to specimens built at near-optimal parameters after HIP. It is also needed to evaluate how much the as-built condition affects the post-HIP fatigue properties.

7. References

[1] K. Moeinfar, F. Khodabakhshi, S. Kashani-bozorg, M. Mohammadi, and A. Gerlich, "A review on metallurgical aspects of laser additive manufacturing (lam): Stainless steels, nickel superalloys, and titanium alloys," *Journal of Materials Research and Technology*, vol. 16, pp. 1029–1068, 2022.

[2] Q. Luo, L. Yin, T. W. Simpson, and A. M. Beese, "Effect of processing parameters on pore structures, grain features, and mechanical properties in ti-6al-4v by laser powder bed fusion," *Additive Manufacturing*, vol. 56, p. 102915, 2022.

[3] S. Kou, *Welding Metallurgy (3rd Edition)*. Knovel ebooks, John Wiley & Sons, Inc., 2020.

[4] L. Thijs, F. Verhaeghe, T. Craeghs, J. V. Humbeeck, and J.-P. Kruth, "A study of the microstructural evolution during selective laser melting of ti–6al–4v," *Acta Materialia*, vol. 58, no. 9, pp. 3303–3312, 2010.

[5] A. du Plessis and E. Macdonald, "Hot isostatic pressing in metal additive manufacturing: X-ray tomography reveals details of pore closure," *Additive Manufacturing*, vol. 34, p. 101191, 2020.

[6] A. Streek, P. Regenfuss, and H. Exner, "Fundamentals of energy conversion and dissipation in powder layers during laser micro sintering," *Physics Procedia*, vol. 41, pp. 858–869, Jan 2013.

[7] H. Lee, C. H. J. Lim, M. J. Low, N. Tham, V. M. Murukeshan, and Y.-J. Kim, "Lasers in additive manufacturing: A review," *International Journal of Precision Engineering and Manufacturing-Green Technology*, vol. 4, pp. 307–322, Jul 2017.

[8] N. K. Tolochko, Y. V. Khlopkov, S. E. Mozzharov, M. B. Ignatiev, T. Laoui, and V. I. Titov, "Absorptance of powder materials suitable for laser sintering," *Rapid Prototyping Journal*, vol. 6, pp. 155–161, Jan 2000.

[9] N. Emminghaus, R. Bernhard, J. Hermsdorf, and S. Kaierle, "Determination of optimum process parameters for different ti-6al-4v powders processed by laser-based powder bed fusion," *Procedia CIRP*, vol. 111, pp. 134–137, 2022. 12th CIRP Conference on Photonic Technologies [LANE 2022].

[10] S. Pal, N. Gubeljak, R. Hudák, G. Lojen, V. Rajťúková, T. Brajlih, and I. Drstvenšek, "Evolution of the metallurgical properties of ti-6al-4v, produced with different laser processing parameters, at constant energy density in selective laser melting," *Results in Physics*, vol. 17, p. 103186, Jun 2020.

[11] J. Campbell, *Complete Casting Handbook*. Elsevier, 2011.

[12] R. E. Reed-Hill, R. Abbaschian, and L. Abbaschian, *Physical metallurgy principles.* Cengage, 4 ed., 2009.

[13] S. Tammas-Williams, P. Withers, I. Todd, and P. Prangnell, "Porosity regrowth during heat treatment of hot isostatically pressed additively manufactured titanium components," *Scripta Materialia*, vol. 122, pp. 72–76, 2016.

[14] R. Cunningham, A. Nicolas, J. Madsen, E. Fodran, E. Anagnostou, M. D. Sangid, and A. D. Rollett, "Analyzing the effects of powder and post-processing on porosity and properties of electron beam melted ti-6al-4v," *Materials Research Letters*, vol. 5, no. 7, pp. 516–525, 2017.

[15] S. Shao, M. J. Mahtabi, N. Shamsaei, and S. M. Thompson, "Solubility of argon in laser additive manufactured α-titanium under hot isostatic pressing condition," *Computational Materials Science*, vol. 131, pp. 209–219, 2017.

[16] T. P. Moran, P. E. Carrion, S. Lee, N. Shamsaei, N. Phan, and D. H. Warner, "Hot isostatic pressing for fatigue critical additively manufactured ti-6al-4v," *Materials*, vol. 15, no. 6, 2022.

[17] J. Alegre, A. D´ıaz, R. Garc´ıa, L. Peral, and I. Cuesta, "Effect of hip post-processing at 850 °c/200 mpa in the fatigue behavior of ti-6al-4v alloy fabricated by selective laser melting," *International Journal of Fatigue*, vol. 163, p. 107097, 2022.

[18] N. E. Dowling, *Mechanical Behavior of Materials*. Pearson, 4 ed., 2013.

[19] H. O. Psihoyos, G. N. Lampeas, and S. G. Pantelakis, "A modelling framework for fatigue-life prediction of selective laser melting additive manufactured ti-6al-4v," *Procedia Structural Integrity*, vol. 34, pp. 253–258, 2021. The second European Conference on the Structural Integrity of Additively Manufactured Materials.

[20] Z. Qu, Z. Zhang, Y. Zhu, R. Liu, S. Lu, S. Li, Q. Duan, B. Zhang, M. Zhao, J. Eckert, and Z. Zhang, "Coupling effects of microstructure and defects on the fatigue properties of laser powder bed fusion ti-6al-4v," *Additive Manufacturing*, vol. 61, p. 103355, 2023.

[21] H. Masuo, Y. Tanaka, S. Morokoshi, H. Yagura, T. Uchida, Y. Yamamoto, and Y. Murakami, "Influence of defects, surface roughness and hip on the fatigue strength of ti-6al-4v manufactured by additive manufacturing," *International Journal of Fatigue*, vol. 117, pp. 163–179, 2018.

[22] T. McKenna, C. Tomonto, G. Duggan, E. Lalor, S. O'Shaughnessy, and D. Trimble, "Evaluation of bimodal microstructures in selective-laser-melted and heat-treated ti-6al-4v," *Materials & Design*, vol. 227, p. 111700, 2023.

[23] S. Leuders, M. Thöne, A. Riemer, T. Niendorf, T. Tröster, H. Richard, and H. Maier, "On the mechanical behaviour of titanium alloy tial6v4 manufactured by selective laser melting: Fatigue resistance and crack growth performance,"

International Journal of Fatigue, vol. 48, pp. 300–307, 2013.

[24] T. Ahmed and H. J. Rack, "Phase transformations during cooling in α+β titanium alloys," *Materials Science and Engineering: A*, vol. 243, pp. 206–211, Mar 1998.

[25] D. Richerson, *Modern Ceramic Engineering: Properties, Processing, and Use in Design, Third Edition*. Taylor & Francis, 3 ed., 11 2006.

[26] Y. Liu, S. Li, H. Wang, W. Hou, Y. Hao, R. Yang, T. Sercombe, and L. Zhang, "Microstructure, defects and mechanical behavior of beta-type titanium porous structures manufactured by electron beam melting and selective laser melting," *Acta Materialia*, vol. 113, pp. 56–67, 2016.

[27] G. Brot, I. Koutiri, V. Bonnand, V. Favier, C. Dupuy, N. Ranc, P. Aimedieu, F. Lefebvre, and R. Hauteville, "Microstructure and defect sensitivities in the very high-cycle fatigue response of laser powder bed fused ti–6al–4v," *International Journal of Fatigue*, vol. 174, p. 107710, 2023.

[28] W. Xu, S. Sun, J. Elambasseril, Q. Liu, M. Brandt, and M. Qian, "Ti-6al-4v additively manufactured by selective laser melting with superior mechanical properties," *JOM*, vol. 67, pp. 668–673, Mar 2015.

[29] H. Ali, L. Ma, H. Ghadbeigi, and K. Mumtaz, "In-situ residual stress reduction, martensitic decomposition and mechanical properties enhancement through high temperature powder bed pre-heating of selective laser melted ti6al4v," *Materials Science and Engineering: A*, vol. 695, pp. 211–220, May 2017.

8. Appendices

A 20 μm size and shape distributions

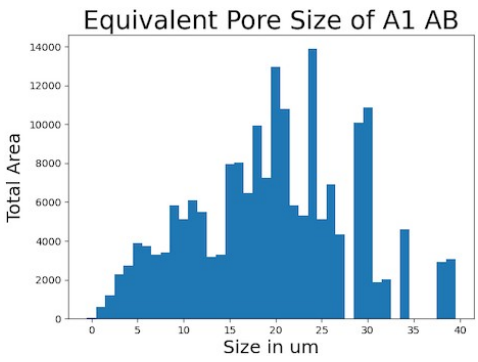

(a)

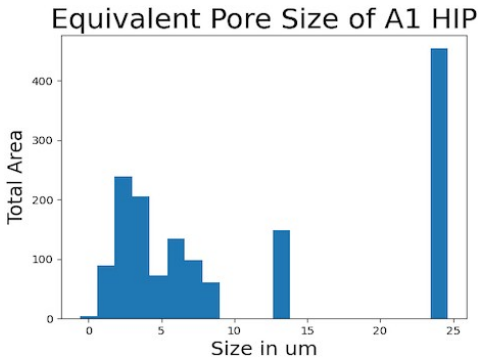

(b)

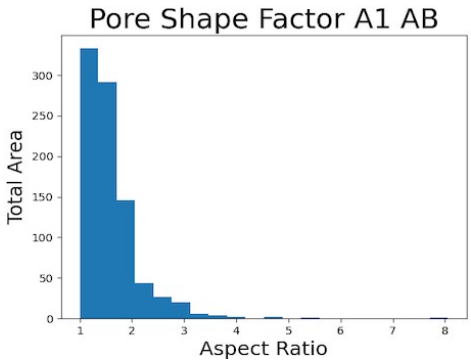

(c)

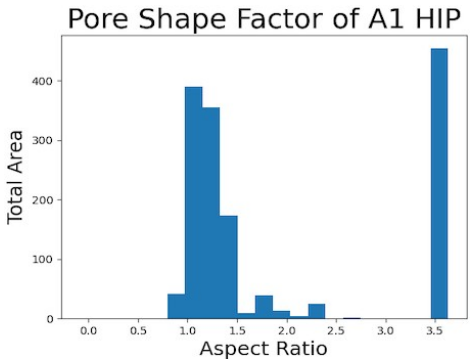

(d)

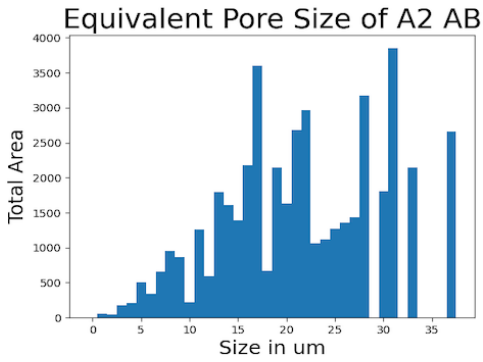
Equivalent Pore Size of A2 AB
Total Area
Size in um

(a)

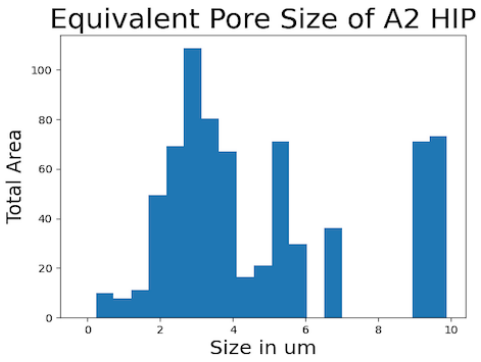
Equivalent Pore Size of A2 HIP
Total Area
Size in um

(b)

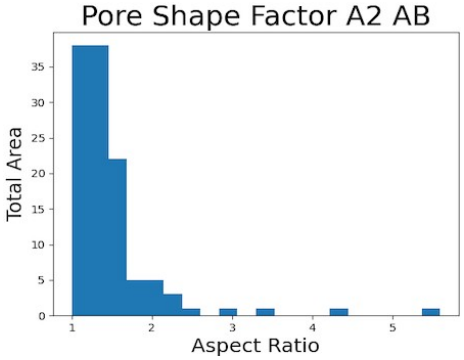
Pore Shape Factor A2 AB
Total Area
Aspect Ratio

(c)

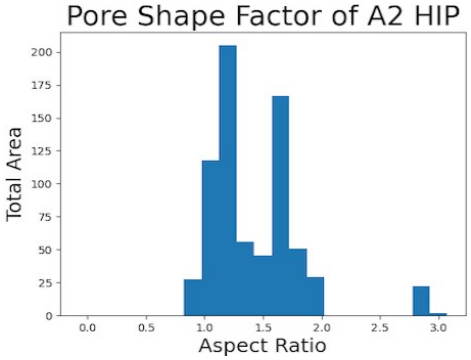
Pore Shape Factor of A2 HIP
Total Area
Aspect Ratio

(d)

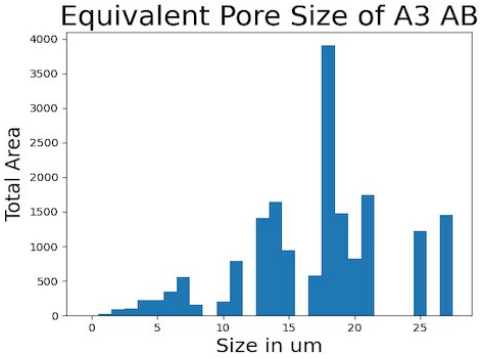
Equivalent Pore Size of A3 AB
Total Area
Size in um

(e)

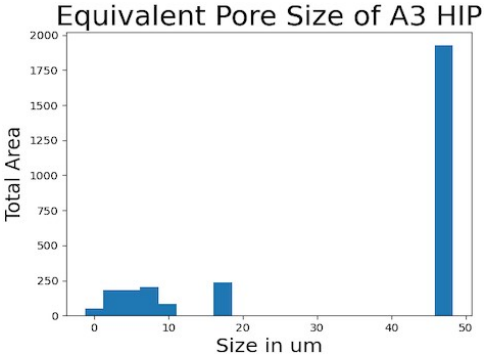
Equivalent Pore Size of A3 HIP
Total Area
Size in um

(f)

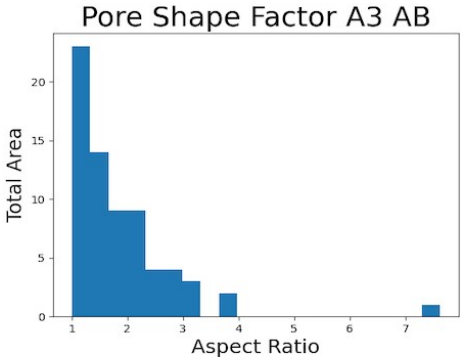
Pore Shape Factor A3 AB
Total Area
Aspect Ratio

(g)

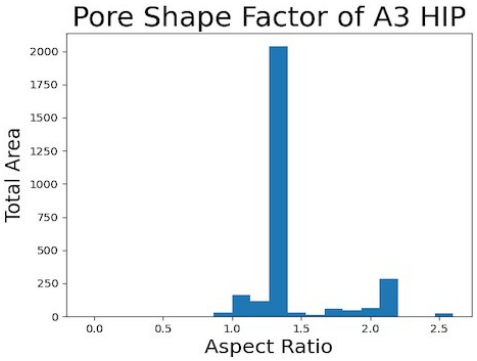
Pore Shape Factor of A3 HIP
Total Area
Aspect Ratio

(h)

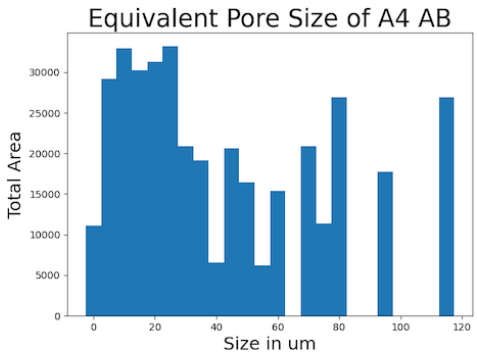
Equivalent Pore Size of A4 AB
Total Area
Size in um

(a)

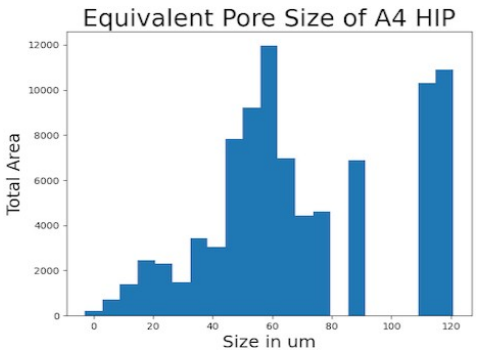
Equivalent Pore Size of A4 HIP
Total Area
Size in um

(b)

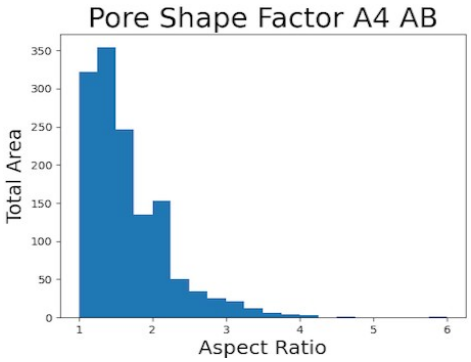
Pore Shape Factor A4 AB
Total Area
Aspect Ratio

(c)

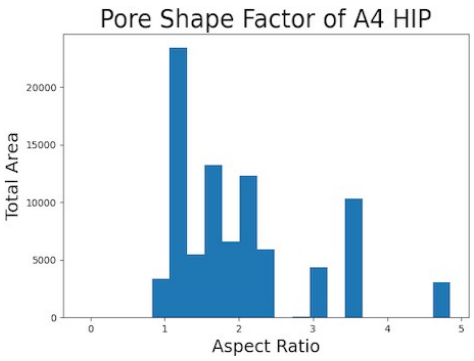
Pore Shape Factor of A4 HIP
Total Area
Aspect Ratio

(d)

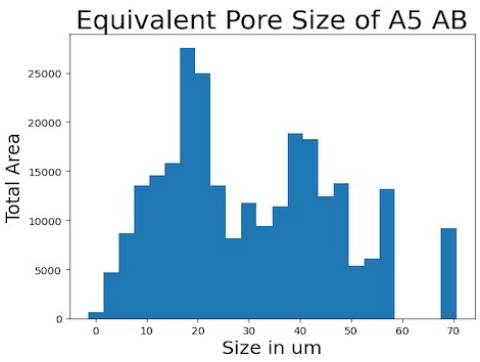
Equivalent Pore Size of A5 AB
Total Area
Size in um

(e)

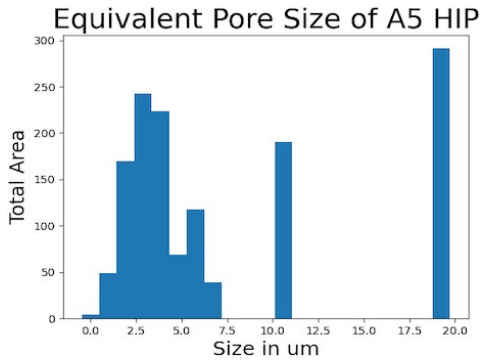
Equivalent Pore Size of A5 HIP
Total Area
Size in um

(f)

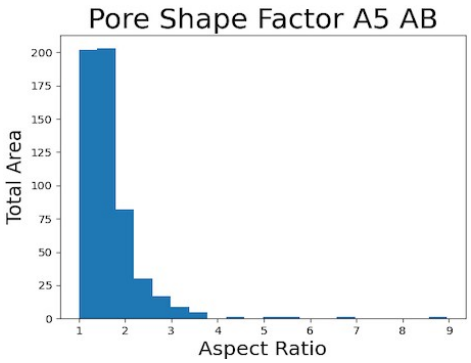
Pore Shape Factor A5 AB
Total Area
Aspect Ratio

(g)

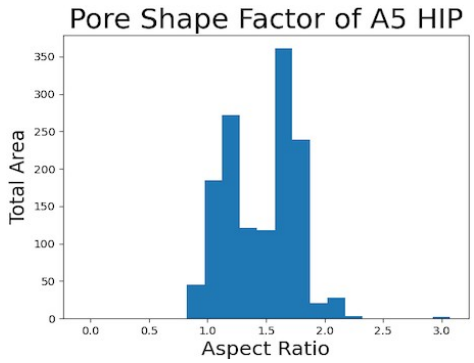
Pore Shape Factor of A5 HIP
Total Area
Aspect Ratio

(h)

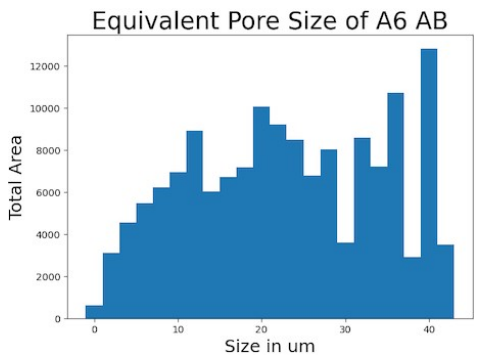
Equivalent Pore Size of A6 AB
Total Area
Size in um

(a)

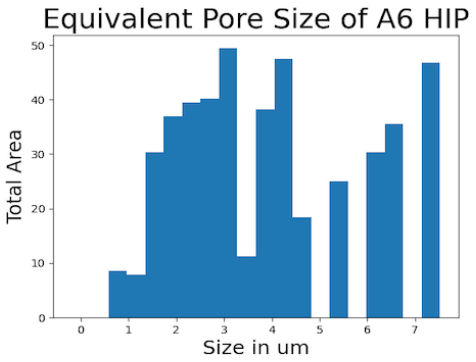
Equivalent Pore Size of A6 HIP
Total Area
Size in um

(b)

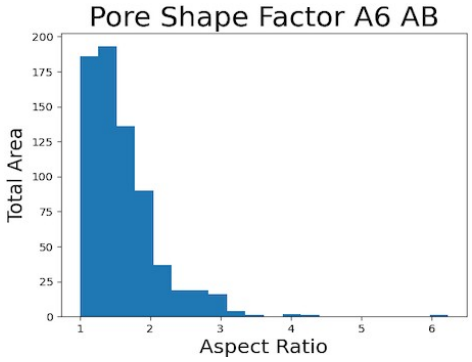
Pore Shape Factor A6 AB
Total Area
Aspect Ratio

(c)

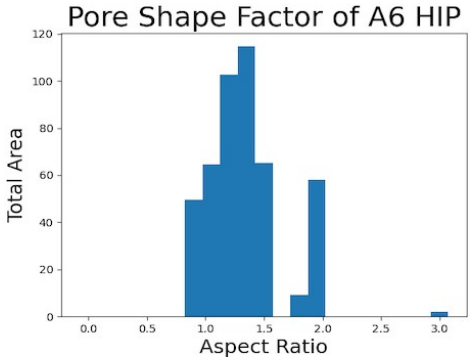
Pore Shape Factor of A6 HIP
Total Area
Aspect Ratio

(d)

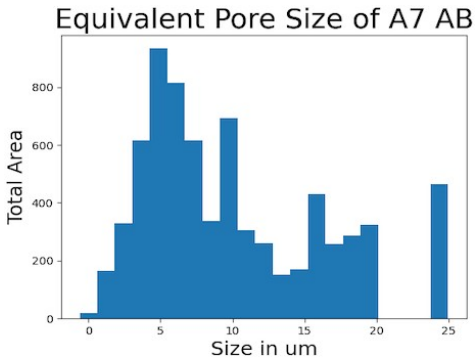
Equivalent Pore Size of A7 AB
Total Area
Size in um

(e)

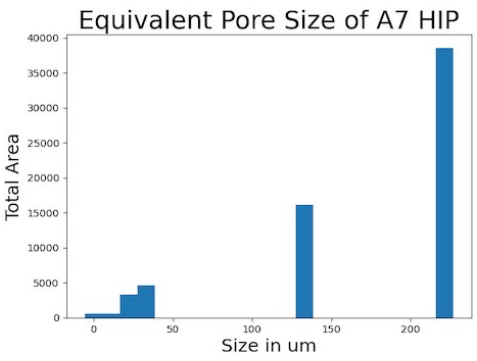
Equivalent Pore Size of A7 HIP
Total Area
Size in um

(f)

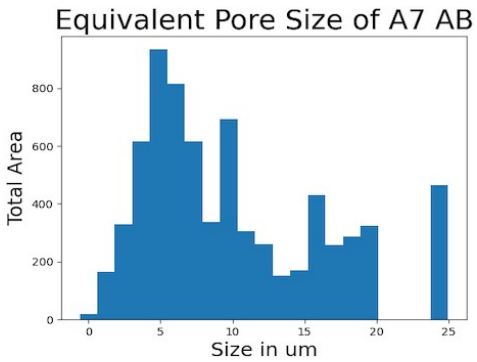
Equivalent Pore Size of A7 AB
Total Area
Size in um

(g)

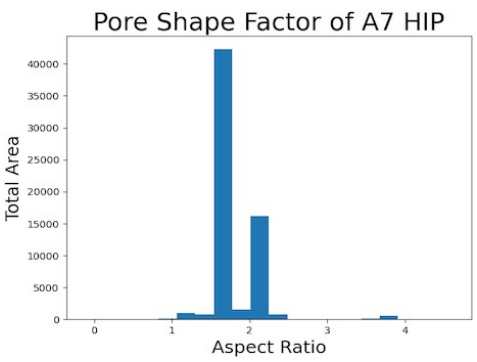
Pore Shape Factor of A7 HIP
Total Area
Aspect Ratio

(h)

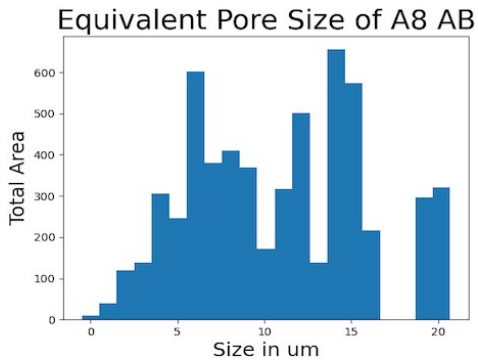
Equivalent Pore Size of A8 AB
Total Area
Size in um

(a)

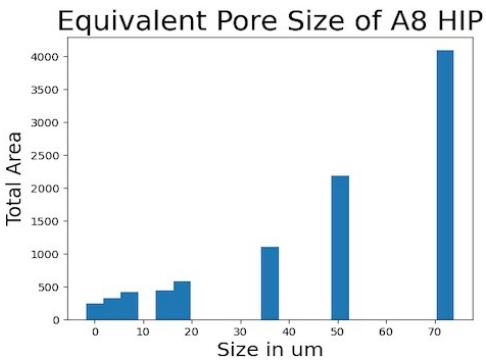
Equivalent Pore Size of A8 HIP
Total Area
Size in um

(b)

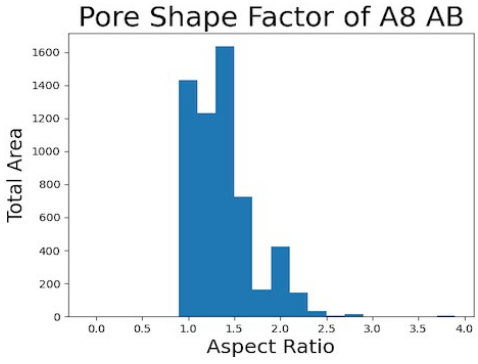
Pore Shape Factor of A8 AB
Total Area
Aspect Ratio

(c)

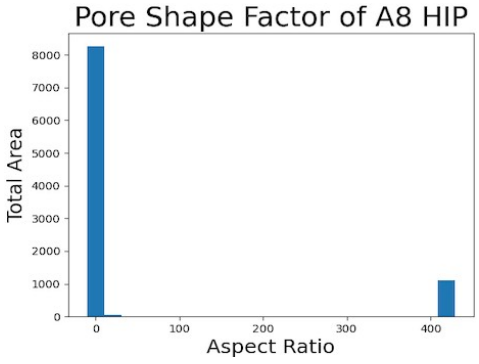
Pore Shape Factor of A8 HIP
Total Area
Aspect Ratio

(d)

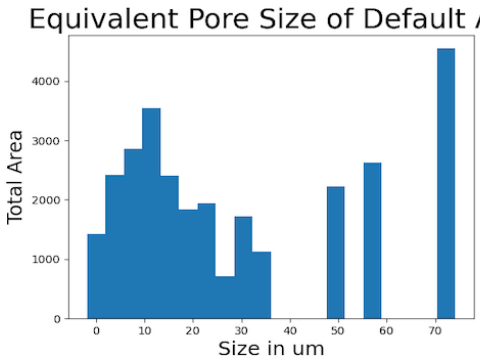
Equivalent Pore Size of Default AB
Total Area
Size in um

(e)

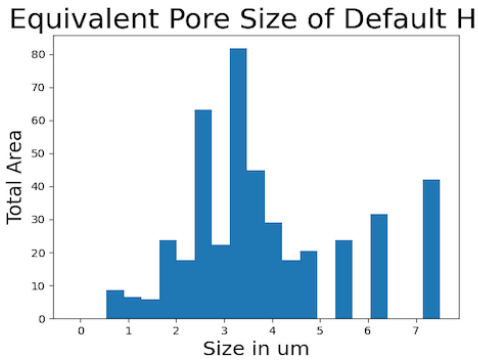
Equivalent Pore Size of Default HIP
Total Area
Size in um

(f)

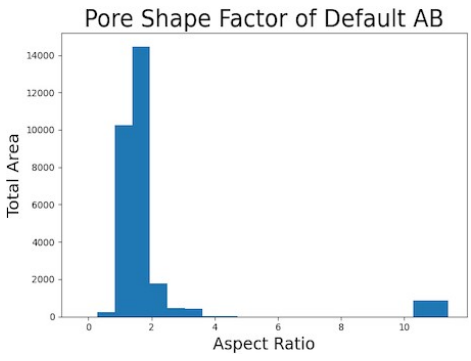
Pore Shape Factor of Default AB
Total Area
Aspect Ratio

(g)

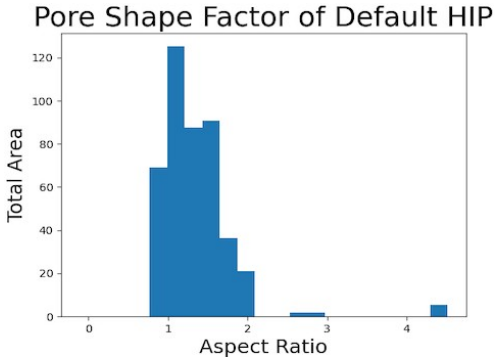
Pore Shape Factor of Default HIP
Total Area
Aspect Ratio

(h)

B 40 μm size and shape distributions

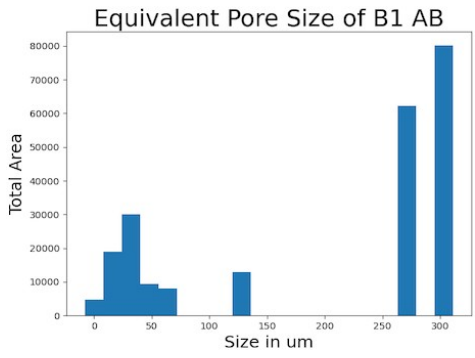

(a)

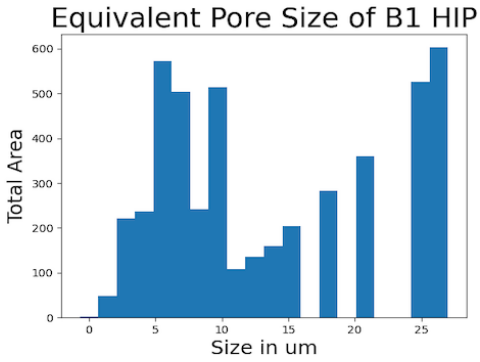

(b)

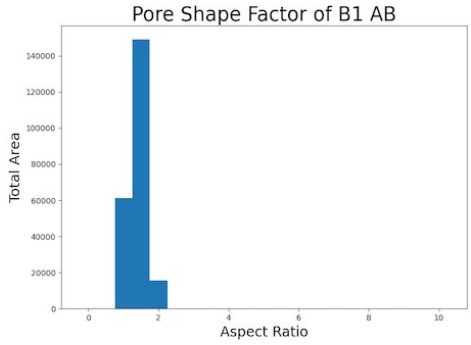

(c)

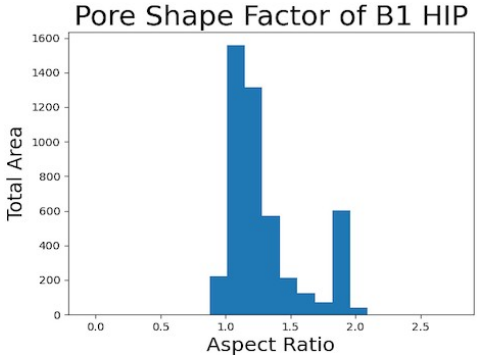

(d)

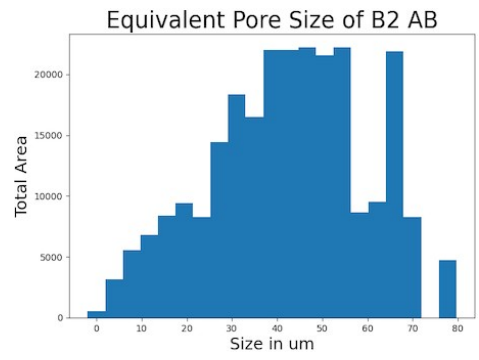
Equivalent Pore Size of B2 AB
Total Area
Size in um

(a)

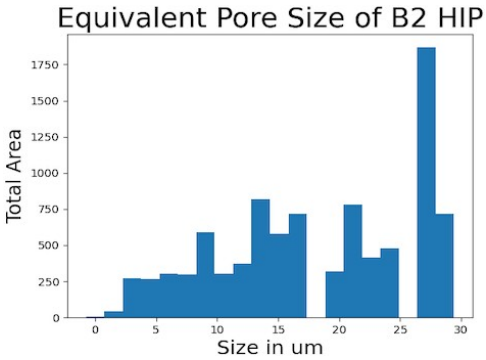
Equivalent Pore Size of B2 HIP
Total Area
Size in um

(b)

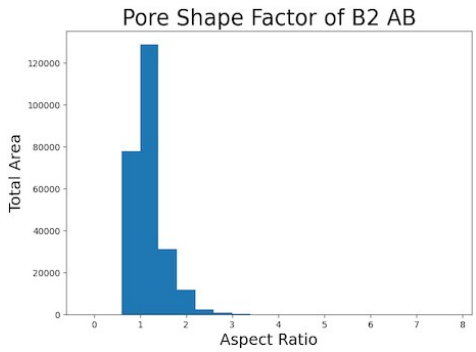
Pore Shape Factor of B2 AB
Total Area
Aspect Ratio

(c)

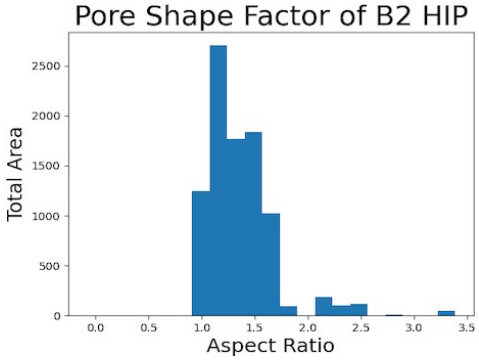
Pore Shape Factor of B2 HIP
Total Area
Aspect Ratio

(d)

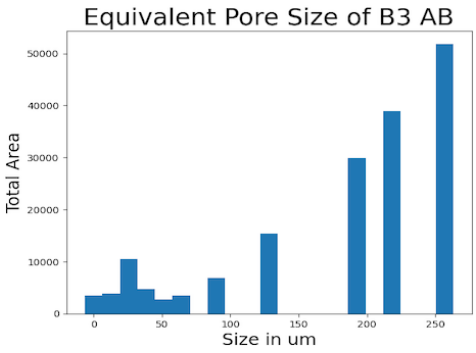
Equivalent Pore Size of B3 AB
Total Area
Size in um

(e)

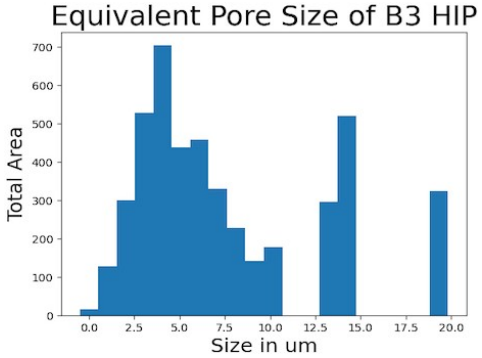
Equivalent Pore Size of B3 HIP
Total Area
Size in um

(f)

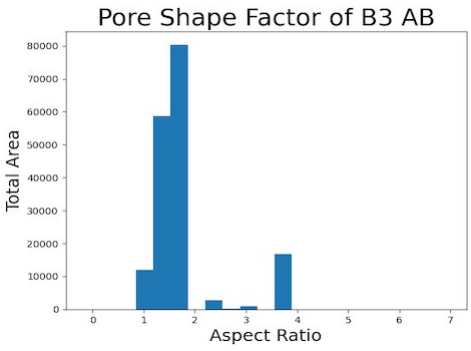
Pore Shape Factor of B3 AB
Total Area
Aspect Ratio

(g)

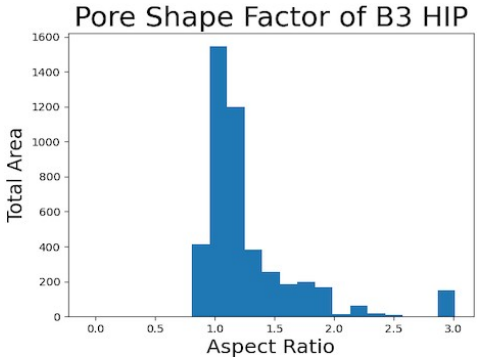
Pore Shape Factor of B3 HIP
Total Area
Aspect Ratio

(h)

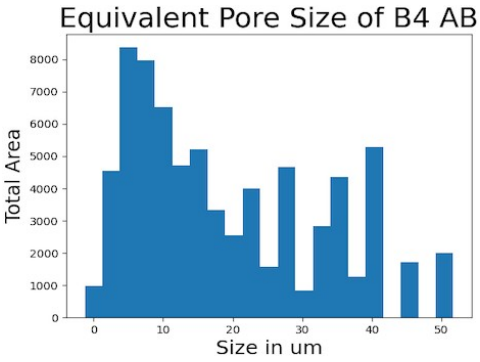
Equivalent Pore Size of B4 AB
Total Area
Size in um

(a)

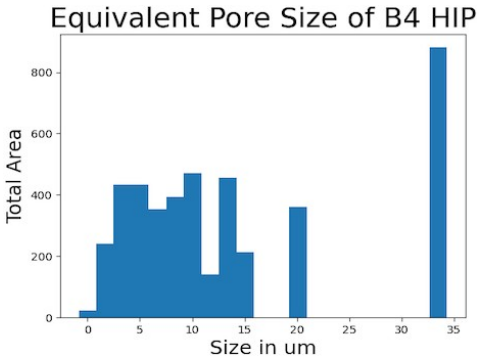
Equivalent Pore Size of B4 HIP
Total Area
Size in um

(b)

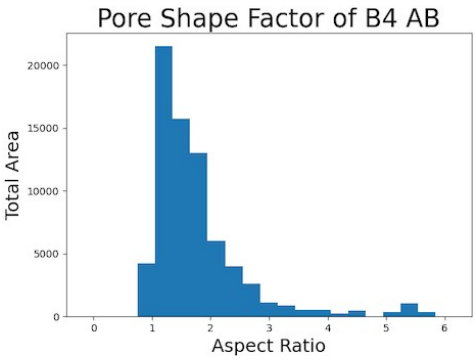
Pore Shape Factor of B4 AB
Total Area
Aspect Ratio

(c)

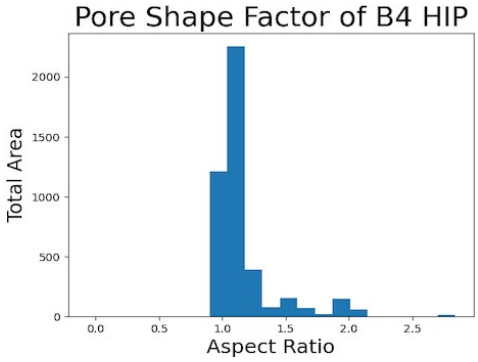
Pore Shape Factor of B4 HIP
Total Area
Aspect Ratio

(d)

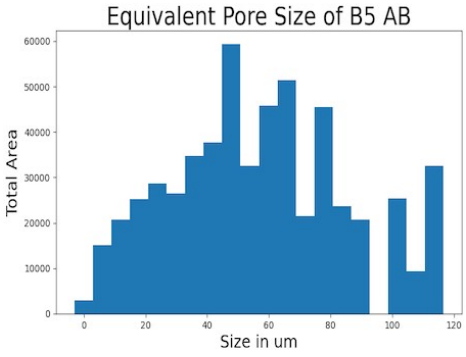
Equivalent Pore Size of B5 AB
Total Area
Size in um

(e)

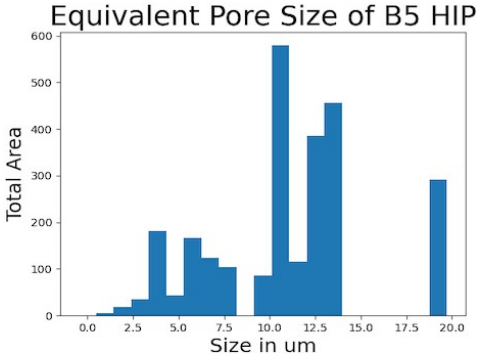
Equivalent Pore Size of B5 HIP
Total Area
Size in um

(f)

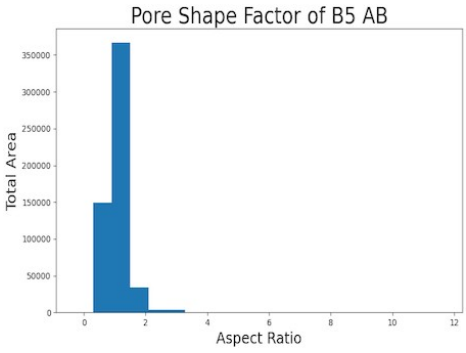
Pore Shape Factor of B5 AB
Total Area
Aspect Ratio

(g)

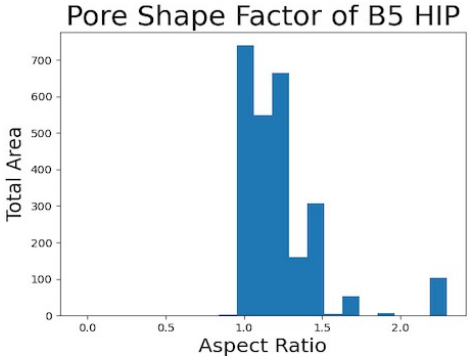
Pore Shape Factor of B5 HIP
Total Area
Aspect Ratio

(h)

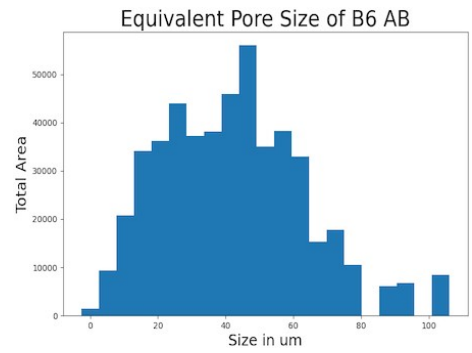
Equivalent Pore Size of B6 AB
Total Area
Size in um

(a)

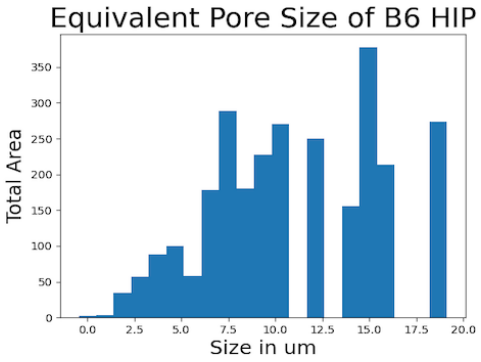
Equivalent Pore Size of B6 HIP
Total Area
Size in um

(b)

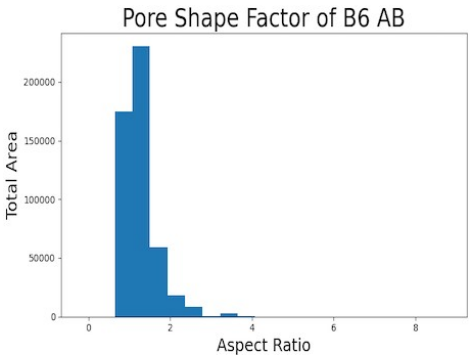
Pore Shape Factor of B6 AB
Total Area
Aspect Ratio

(c)

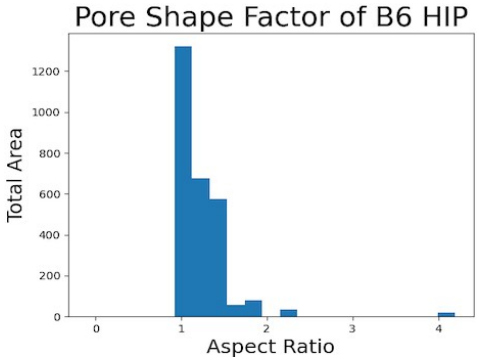
Pore Shape Factor of B6 HIP
Total Area
Aspect Ratio

(d)

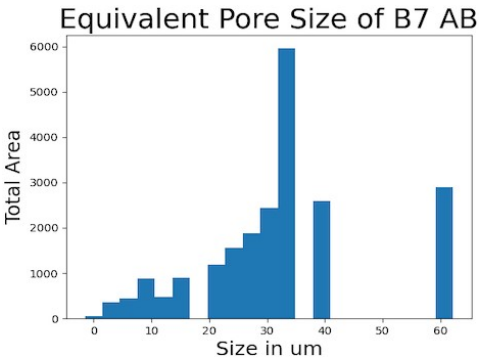
Equivalent Pore Size of B7 AB
Total Area
Size in um

(e)

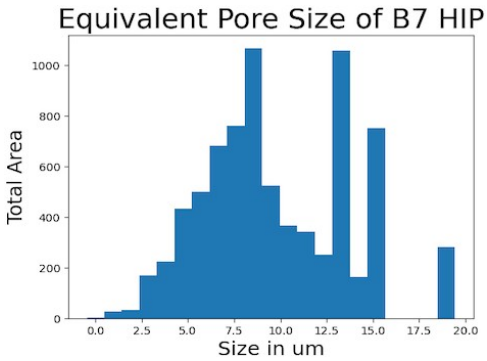
Equivalent Pore Size of B7 HIP
Total Area
Size in um

(f)

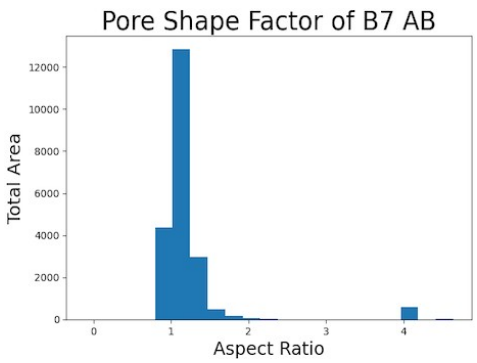
Pore Shape Factor of B7 AB
Total Area
Aspect Ratio

(g)

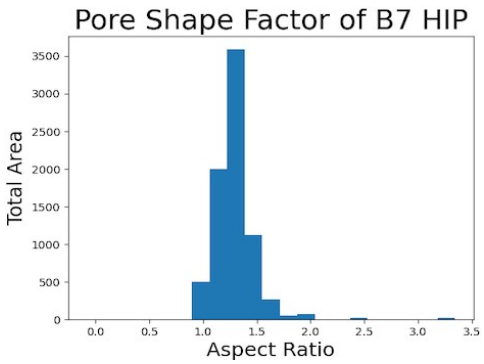
Pore Shape Factor of B7 HIP
Total Area
Aspect Ratio

(h)

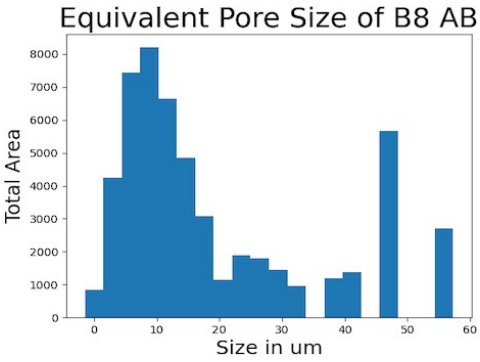
Equivalent Pore Size of B8 AB
Total Area
Size in um

(a)

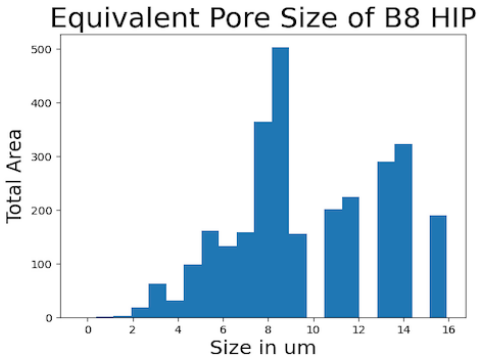
Equivalent Pore Size of B8 HIP
Total Area
Size in um

(b)

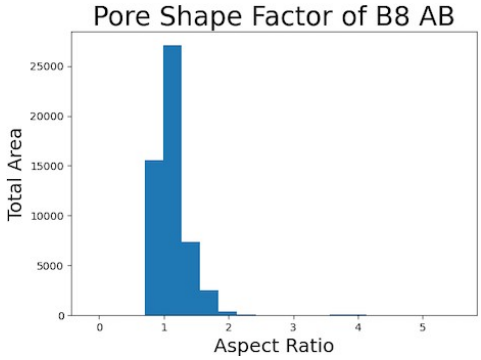
Pore Shape Factor of B8 AB
Total Area
Aspect Ratio

(c)

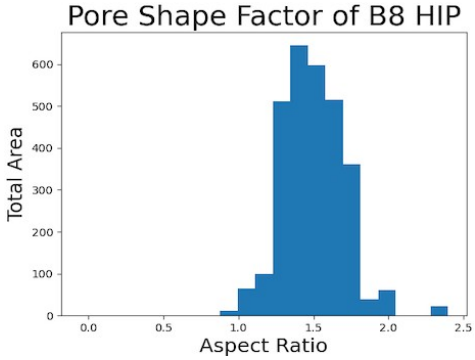
Pore Shape Factor of B8 HIP
Total Area
Aspect Ratio

(d)

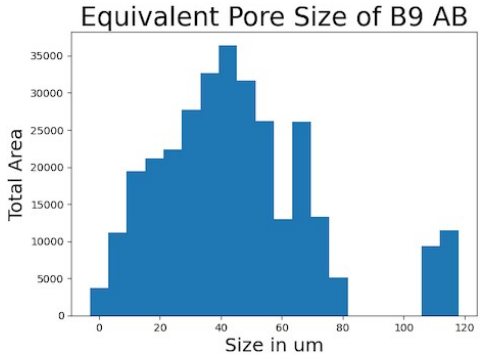
Equivalent Pore Size of B9 AB
Total Area
Size in um

(e)

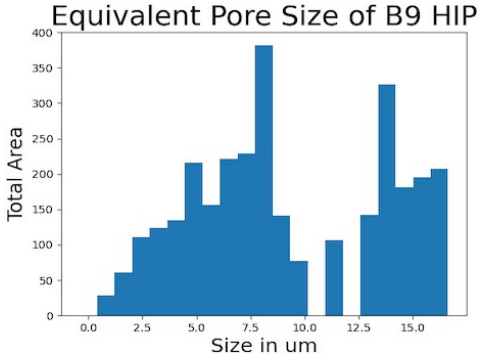
Equivalent Pore Size of B9 HIP
Total Area
Size in um

(f)

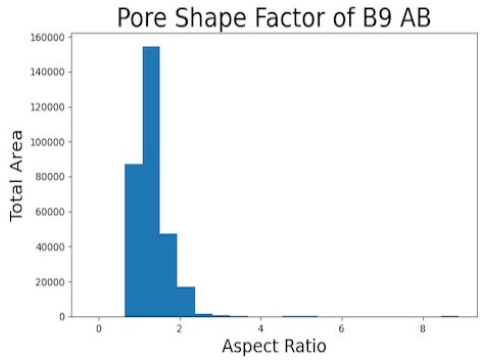
Pore Shape Factor of B9 AB
Total Area
Aspect Ratio

(g)

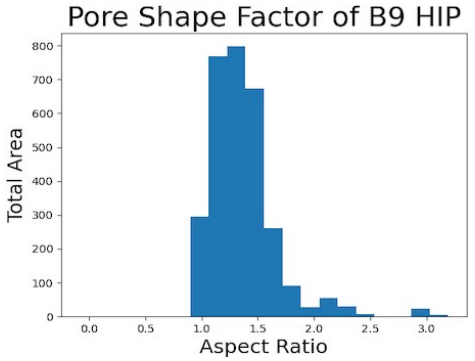
Pore Shape Factor of B9 HIP
Total Area
Aspect Ratio

(h)

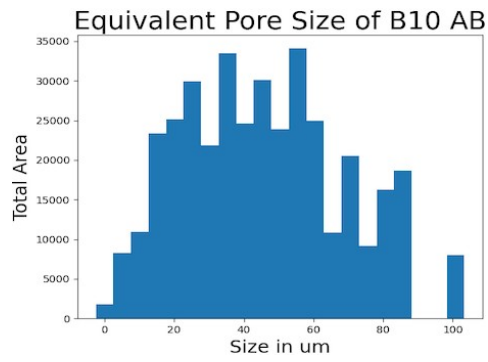
Equivalent Pore Size of B10 AB
Total Area
Size in um

(a)

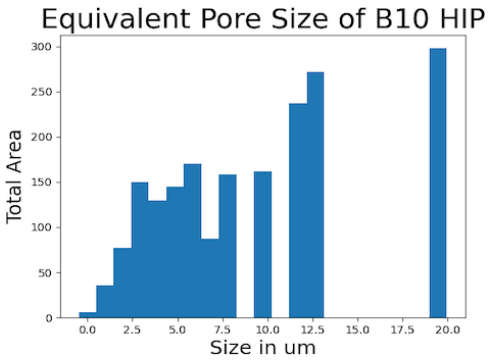
Equivalent Pore Size of B10 HIP
Total Area
Size in um

(b)

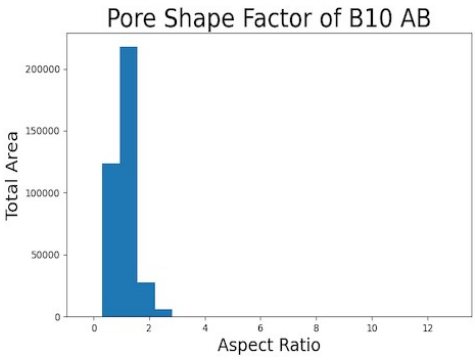
Pore Shape Factor of B10 AB
Total Area
Aspect Ratio

(c)

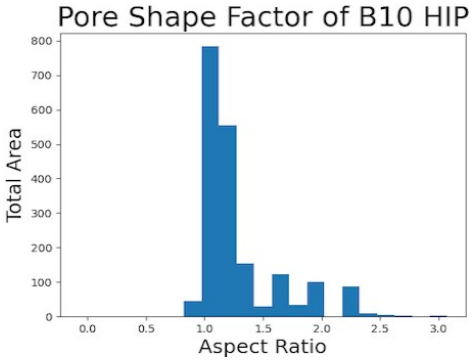
Pore Shape Factor of B10 HIP
Total Area
Aspect Ratio

(d)

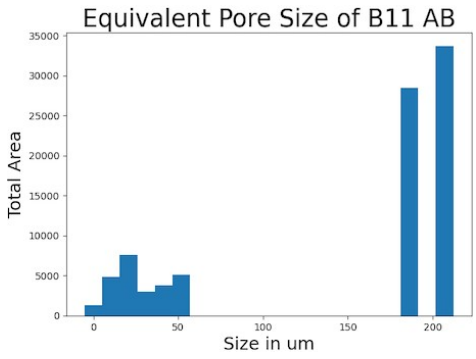
Equivalent Pore Size of B11 AB
Total Area
Size in um

(e)

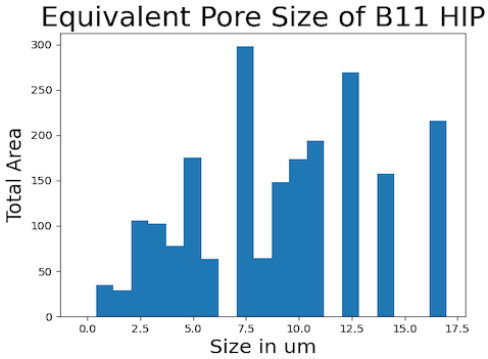
Equivalent Pore Size of B11 HIP
Total Area
Size in um

(f)

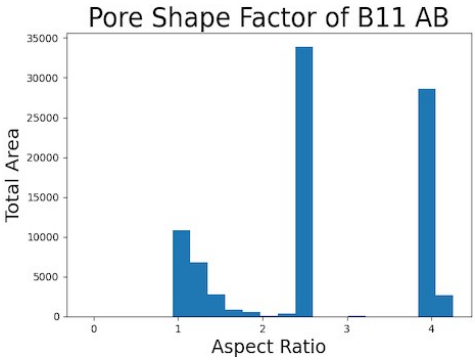
Pore Shape Factor of B11 AB
Total Area
Aspect Ratio

(g)

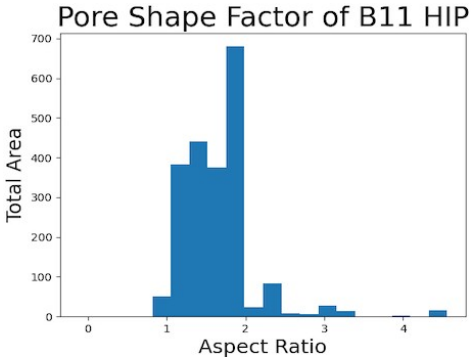
Pore Shape Factor of B11 HIP
Total Area
Aspect Ratio

(h)

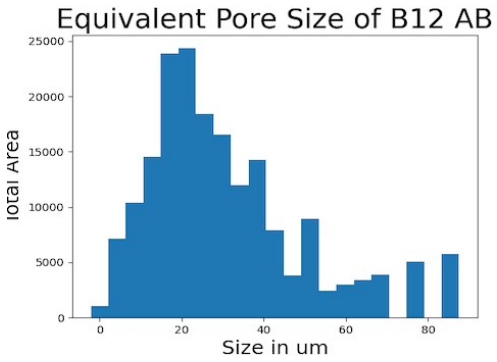
Equivalent Pore Size of B12 AB
Total Area
Size in um

(a)

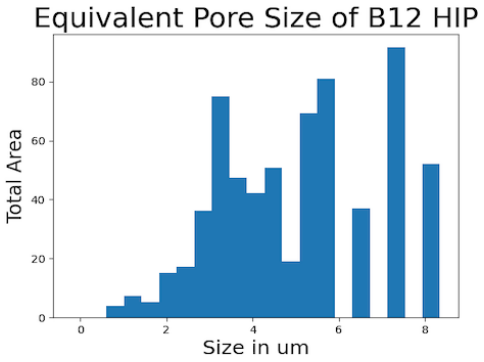
Equivalent Pore Size of B12 HIP
Total Area
Size in um

(b)

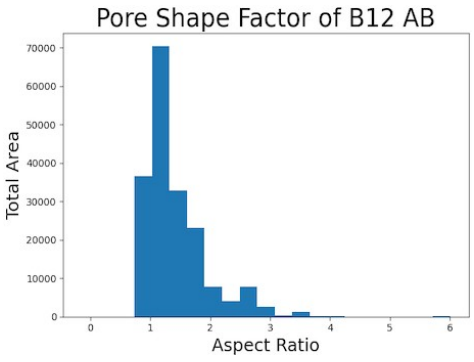
Pore Shape Factor of B12 AB
Total Area
Aspect Ratio

(c)

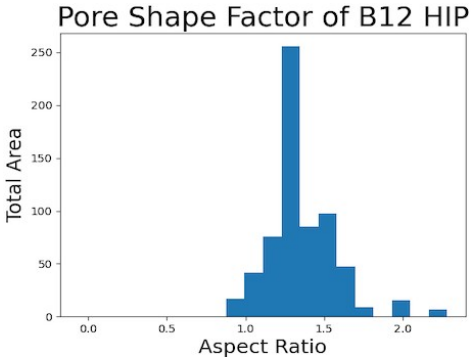
Pore Shape Factor of B12 HIP
Total Area
Aspect Ratio

(d)

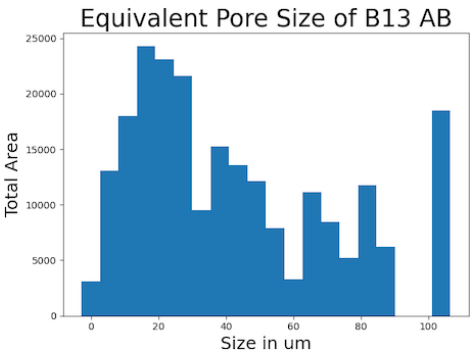
Equivalent Pore Size of B13 AB
Total Area
Size in um

(e)

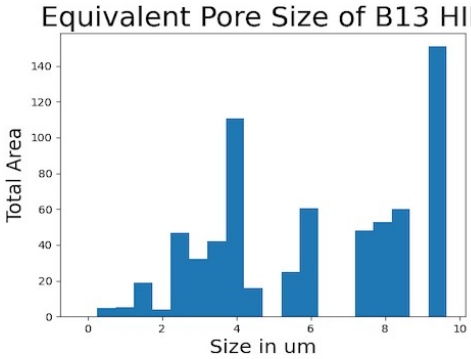
Equivalent Pore Size of B13 HIP
Total Area
Size in um

(f)

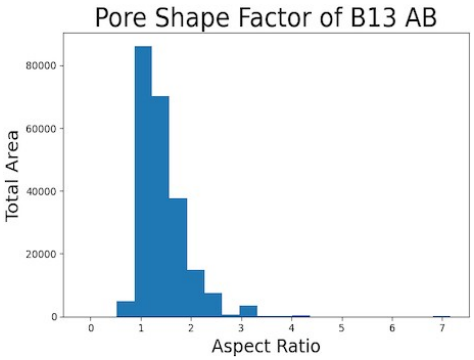
Pore Shape Factor of B13 AB
Total Area
Aspect Ratio

(g)

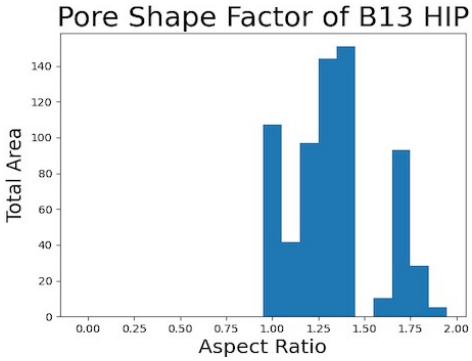
Pore Shape Factor of B13 HIP
Total Area
Aspect Ratio

(h)